FABRICATION AND CHARACTERIZATION OF UPCONVERTING RF MAGNETRON SPUTTERED YTTERBIUM-ERBIUM SILICATE THIN FILMS

A THESIS SUBMITTED TO
THE GRADUATE SCHOOL OF NATURAL AND APPLIED SCIENCES
OF
MIDDLE EAST TECHNICAL UNIVERSITY

BY

MUHAMMET MUSTAFA ÇODUR

IN PARTIAL FULFILLMENT OF THE REQUIREMENTS
FOR
THE DEGREE OF MASTER OF SCIENCE
IN
MICRO AND NANOTECHNOLOGY

APRIL 2020

Approval of the thesis:

FABRICATION AND CHARACTERIZATION OF UPCONVERTING RF MAGNETRON SPUTTERED YTTERBIUM-ERBIUM SILICATE THIN FILMS

submitted by **MUHAMMET MUSTAFA ÇODUR** in partial fulfillment of the requirements for the degree of **Master of Science** i**n Micro and Nanotechnology, Middle East Technical University** by,

Prof. Dr. Halil Kalıpçılar
Dean, Graduate School of **Natural and Applied Sciences** _____

Prof. Dr. Almıla Güvenç Yazıcıoğlu
Head of the Department, **Micro and Nanotechnology** _____

Assist. Prof. Dr. Selçuk Yerci
Supervisor, **Micro and Nanotechnology, METU** _____

Assoc. Prof. Dr. İpek Güler
Co-Supervisor, **Inter-Curricular Courses Dept., Çankaya Uni.** _____

Examining Committee Members:

Assoc. Prof. Dr. Alpan Bek
Physics, METU _____

Assist. Prof. Dr. Selçuk Yerci
Micro and Nanotechnology, METU _____

Assoc. Prof. Dr. İpek Güler
Inter-Curricular Courses Dept., Çankaya Uni. _____

Assist. Prof. Dr. Kuroş Salimi
Chemical Eng., Yıldırım Beyazıt Uni. _____

Assist. Prof. Dr. Emre Yüce
Physics, METU _____

Date: 06.04.2020

I hereby declare that all information in this document has been obtained and presented in accordance with academic rules and ethical conduct. I also declare that, as required by these rules and conduct, I have fully cited and referenced all material and results that are not original to this work.

Name, Last name : Muhammet Mustafa, Çodur

Signature :

ABSTRACT

FABRICATION AND CHARACTERIZATION OF UPCONVERTING RF MAGNETRON SPUTTERED YTTERBIUM-ERBIUM SILICATE THIN FILMS

Çodur, Muhammet Mustafa
Master of Science, Micro and Nanotechnology
Supervisor: Assist. Prof. Dr. Selçuk Yerci
Co-Supervisor: Assoc. Prof. Dr. İpek Güler

April 2020, 64 pages

Upconversion is a growing research topic as it can be utilized in various applications extending from traditional fields, such as solar cells, and infrared sensing to novel fields, including bioimaging and 3D displays. However, heavy halides, which are frequently used as upconversion host matrices in the literature, exhibit unstable chemical, mechanical, and thermal properties. Oxides with high stability can be used as an alternative to heavy halides, but their high phonon energy reduces upconversion efficiency. In this study, we aimed to enhance the efficiency by increasing the number of luminescence centers (i.e. erbium ions) in the host matrix by utilizing erbium ions as constituents of the compound instead of doping ions. This thesis is dedicated to the improvement of upconversion properties of erbium-ytterbium disilicate ($Er_xYb_{2-x}Si_2O_7$) compounds as an upconversion material with stable properties. Herein, sputtering was preferred as the fabrication method not only for its uniform deposition capability but also for its compatibility with the silicon technology.

In this thesis, we demonstrated erbium-ytterbium disilicate thin films that convert infrared photons with a wavelength from around 1540 nm into a wavelength of around 980 nm. Moreover, the effects of annealing temperature and, erbium and ytterbium concentrations on the upconversion efficiency were investigated. Noteworthy, we present upconversion from erbium-ytterbium silicates as thin as 110 nm. All films fabricated in this work show pure NIR-NIR upconversion, which is considered to be more favorable in various applications where precision is more requisite than high conversion efficiency in the literature, such as bioimaging and fingerprint detection. They can also be the sought-after material for new applications, for instance, coupling them with a cheap silicon detector to detect photons beyond 1.1 μm. In addition, we enhance a method to measure PL lifetimes of samples. This method combines square wave excitation and a lock-in amplifier and allows real-time lifetime measurements.

Keywords: Upconversion, Erbium-Ytterbium Disilicates, PL Lifetime

ÖZ

RF KATOT PÜSKÜRTME METODU İLE ÜRETİLMİŞ ÜST-ÇEVRİM YAPAN İTERBİYUM-ERBİYUM SİLİKATE İNCE FİLMLERİN FABRİKASYONU VE KARAKTERİZASYONU

Çodur, Muhammet Mustafa
Yüksek Lisans, Mikro ve Nanoteknoloji
Tez Yöneticisi: Dr. Öğr. Üyesi Selçuk Yerci
Ortak Tez Yöneticisi: Doç. Dr. İpek Güler

Nisan 2020, 64 sayfa

Üst-çevrim; güneş pilleri, kızılötesi algılama gibi geleneksel alanlardan biyolojik görüntüleme ve üç boyutlu ekranlar gibi yenilikçi alanlara uzanan geniş bir yelpazede uygulama alanı bulan bir araştırma konusudur. Ancak, literatürde genellikle üst-çevrim ana matrisleri olarak kullanılan ağır halojenürler kararsız kimyasal, mekanik ve termal özellikler sergilerler. Ağır halojenürlere alternatif olarak kullanılabilecek yüksek kararlılığa sahip oksitlerin ise yüksek fonon enerjilerinden dolayı üst-çevrim verimliliği düşüktür. Bu nedenle bizde ana matristeki ışıma merkezlerinin (erbiyum iyonları) sayısını artırarak yani katkı iyonları olarak kullanmak yerine bileşiğin bileşenleri olarak erbium iyonlarını kullanarak verimliliği arttırmayı amaçladık. Bu tezde kararlı özelliklere sahip erbiyum-iterbiyum disilikat ($Er_xYb_{2-x}Si_2O_7$) bileşiklerinin üst-çevrim özelliklerinin geliştirilmesi araştırılmıştır. Burada ayrıca, ince filmlerin üretiminde katot püskürtme metodu sadece tüm yüzeyde eşit biriktirme kabiliyeti için değil ayrıca silikon teknolojisiyle de uyumlu olduğu için de tercih edilmiştir

Bu tezde 1540 nm'den dalga boyuna sahip kızılötesi fotonları 980 nm dalga boyuna dönüştüren erbium-ytterbium disilikat ince filmler üretildi. Tavlama sıcaklığı ile erbiyum ve iterbiyum konsantrasyonlarının üst-çevrim verimliliği üzerindeki etkileri araştırıldı. Bunların sonucunda, 110 nm kadar ince erbium-ytterbium silikatlardan üst-çevrim elde edilmiş ve sonuçlar tez içerisinde verilmiştir. Ayrıca, bu çalışmada üretilen tüm filmler saf yakın kızılötesi ışıması (YKI)-YKI yukarı dönüşümü göstermiştir ve bu dönüşüm biyolojik görüntüleme ve parmak izi tespiti gibi literatürde yüksek dönüşüm verimliliğindense hassasiyetin daha fazla önemli olduğu düşünülen çeşitli uygulamalarda tercih edilir. Tüm bunların dışında yeni uygulamalar için de çok kullanışlı malzemeler olabilirler, örneğin bunlar ucuz bir silisyum tabanlı dedektörle birleştirip 1.1 μm'nin üzerindeki fotonları tespit etmek için kullanılabilirler. Üst-çevrim çalışmalarına ek olarak, bu tez kapsamında üretilen numunelerin PL ömürlerini ölçmek için de bir yöntem geliştirildi. Bu yöntem sayesinde kare dalga uyarımı ve bir kilit amplifikatörü bir arada kullanılabilir ve kare dalga uyarımı ile gerçek zamanlı yaşam süresi ölçülebilir.

Anahtar Kelimeler: Üst-çevrim, erbiyum-iterbiyum disilikat, Fotolüminesans Yaşam Süresi

To my mother

ACKNOWLEDGMENTS

This thesis became a reality with scientifically and morally supports of many individuals. I would like to extend my sincere thanks all of them.

Foremost, I would like to express my deepest gratitude to my supervisor Professor Selçuk Yerci, for giving me the opportunity to do my M.S. in his group, his patience and his guidance. And also, I would like to thank my co-supervisor Professor İpek Koçer Güler for her kind help.

Many thanks to present and past members of Advanced Photonics and Photovoltaics group, for their friendship and continuous support during my studies. I am particularly grateful to Milad Ghasemi for always being very helpful in the lab. I would also express my gratefulness to Mehmet Koç for all the technical discussions we had.

My sincere thanks go to Hüseyin Umut Tepe, Bahri Eren Uzuner, Hassan Osman for constructive criticism of the manuscript and valuable feedbacks in the thesis writing process.

Finally, I am very grateful to my family; my mother, my brother and my sisters who always stand by me with so much love.

This work is funded by TUBITAK under the contract number 116F104.

TABLE OF CONTENTS

LIST OF TABLES

TABLES

LIST OF FIGURES

FIGURES

LIST OF ABBREVIATIONS

ABBREVIATIONS

3D	Three dimensional
SQ	Shockley-Quisser
NIR	Near-infrared
PL	Photoluminescence
UCNPs	Upconversion nanophosphors
FIR	Fluorescence intensity ratios
CR	Cross-relaxation
ESA	Excited state absorption
GSA	Ground state absorption
ETU	Energy transfer upconversion
SEM	Scanning electron microscopy
XRD	X-ray diffraction
CMOS	Complementary metal oxide semiconductor

CHAPTER 1

INTRODUCTION

1.1 Motivation

Upconversion can be defined as generating photon emission with higher energies than excitation photon energy. The upconversion phenomenon in a lanthanide ion for a solid-state infrared quantum counter was first suggested by Bloembergen in 1959 [1]. Since then, due to their numerous applications, the development of the upconversion materials has gathered considerable attention. Some of upconversion applications are solar energy harvesting [2], bioimaging [3], [4], lasers [5], thermal sensors [6], infrared sensing [7], [8], and novel displays [9].

1.1.1 Applications

1.1.1.1 Solar Energy Harvesting

Semiconductors do not absorb photons with energies below their bandgap. However, photons with energies above the bandgap are absorbed, and the excess energy is dissipated as heat and does not contribute to carrier generation. These loss mechanisms are known as transparency and thermalization. Because the solar spectrum consists of photons with a wide range of energies, it does not well match with absorption spectra of a semiconductor. The difference between the energy of the bandgap and solar spectrum is commonly referred to spectral mismatch in the literature. These losses that are fundamental loss mechanisms for single-junction solar cells and cause losses of about 50 % in efficiency [10], as shown in Figure 1.1. To overcome the spectral mismatch, several techniques have been suggested, such as tandem structures (the most popular, the most expensive and the hardest to realize)

[11]–[13], multiple exciton generation [14], intermediate band gaps [15] and lastly, spectral converters [2], [16], [17].

Single-junction crystalline silicon solar cells dominate today's photovoltaic market, and they share more than 90 % [18]-[20]. However, the technology has been approaching the Shockley–Queisser (SQ) limit of 31% [21] with an efficiency record at 26.7 % [22], [23]. One of the major efficiency limiting factors is transparency loss. Photons with smaller energy than the band gap energy of crystalline silicon (1.1 eV) constitute about 20 % in the whole solar spectrum for the standard AM1.5 Global spectrum [24]. The sub-band gap photons can be absorbed by employing upconversion, and the efficiency increases beyond the SQ limit [25], [26]. Calculations show that upconversion could raise the SQ limit to around 38 % [27].

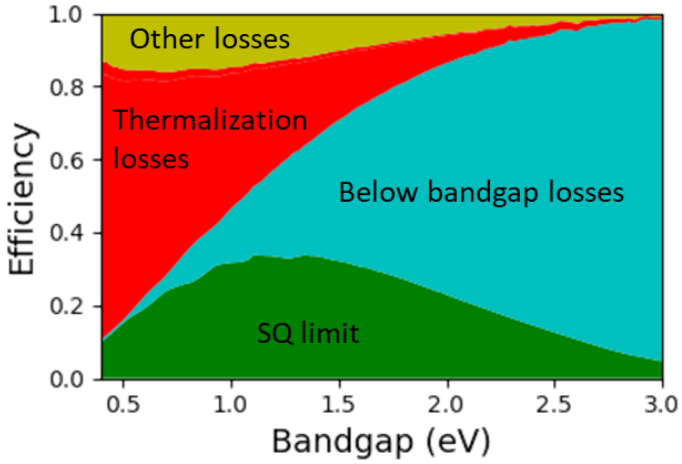

Figure 1.1. The major loss mechanisms in the Shockley- Queisser limit [21]

Figure 1.2 illustrates schematic design of a solar cell with upconversion and reflector layers. An upconverter layer covers the back of the bifacial solar cell, which in turn has a reflector placed at its back to enhance optical coupling. Since the upconverter layer is placed at the rear of the solar cell, incident light is not affected, and the efficiency of the solar cell always increases compared to a bare solar cell (without the upconversion layer).

Goldschmidt et al. published one of the most extensive reviews on upconversion performance in solar cells [28]. Based on this study, the same group has achieved a record short current enhancement of 0.55±0.14% for silicon solar cells under 94±17% suns concentration compared to bare silicon solar cell [29].

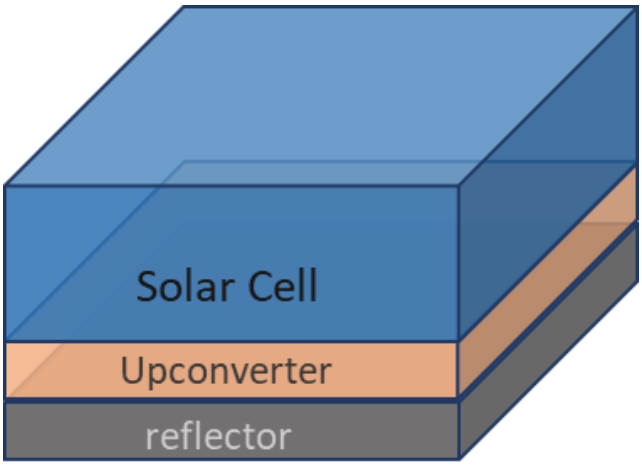

Figure 1.2. Schematic design of a solar cell with upconversion and reflector layers

1.1.1.2 Biological Imaging

Biological imaging (bioimaging) covers non-invasively imaging techniques that visualize biological structures or monitor biological activities. Three-dimensional (3D) structure of the samples are scanned without physical interaction, and without affecting the life processes of organisms. Unlike other techniques, such as magnetic resonance imaging, positron emission tomography, X-ray computed tomography, fluorescence imaging does not exhibit any harmful radioactivity [30]. Fluorescence imaging utilizes an optical comparison of cells between areas with and without fluorophores.

The most studied fluorophores are quantum dots, organic molecules, and upconversion nanophosphors (UCNPs) [31]. While the first two types of fluorophores exhibit Stokes emission, UCNPs enable both Stokes and anti-Stokes emission. Because the optical excitation at the ultraviolet or visible range may excite

the surrounding biological tissues, the use of fluorophores that exhibit Stokes emission is unfavorable. The natural luminescence caused by the surrounding biological tissues is the source of the background noise in bio-imaging, it is called as autofluorescence. In addition to autofluorescence, organic molecules suffer from drawbacks such as photobleaching, broadband emission spectra, degradation [32], [33]. As for quantum dots, they have promising properties such as size-dependent tunable emission wavelength and narrow emission bands. However, they suffer from photoblinking and cytotoxicity [34]. Photoblinking makes continuous real-time imaging difficult and reduces brightness [35]–[37].

In contrast, UCNPs have sought-after properties such as good biocompatibility, continuous luminescence, and photostability [38]. Moreover, UCNPs can be excited with infrared light that has lower energy. Since most biological tissues do not absorb infrared light, the probe beam causes much less damage to the tissues and penetrates into deeper regions of an organism. It also reduces the noise caused by natural luminescence of biological tissues and scattering of the beam (less scattering at long wavelengths). As another option, UCNPs exhibit Stokes-type emission (downconversion) from infrared light excitation, which is not possible with the molecules. Cao et al. [39] made a comparative study on upconversion and downconversion fluorescence for bioimaging. They employed $NaYF_4$: Yb, Tm and $LiLuF_4$: Nd core−shell nanoparticles to make upconversion and downconversion at the infrared range. The nanoparticle emits at 800 nm and 1060 nm when excited by 808 nm and 980 nm, respectively. They found that both methods have similar performance. The only difference between them is that downconversion leads to less heating.

1.1.1.3 Infrared Sensing

Near-infrared (NIR) wavelengths cover the region of the electromagnetic spectrum between 750 nm and 2500 nm, and there are wide varieties of technologies work in that range from analysis of food products to astronomical spectroscopy and 3D

sensing. Therefore, there are numerous studies on the improvement of infrared detectors. Infrared detectors are classified into two types according to their working principles. They are thermal detectors and semiconductor-based photon detectors. While thermal detectors suffer from low temporal resolution, photodetectors are limited by Johnson–Nyquist noise due to their low bandgap energies, which is the thermal background radiation. Alternatively, anti-Stokes processes have been introduced to the NIR detection with silicon-based detectors [40], [41]. Here, either conventional processes such as second harmonic generation and multiphoton absorption or upconversion can be used as an anti-Stokes mechanism in order to shift the infrared light to a shorter wavelength, within the bandgap of silicon. The use of silicon detector reduces both the noise sources associated with infrared detection and costs. To our knowledge, there is no study on lanthanide-based upconverter to detect the NIR light, because of the narrow absorption peaks (the reason of the narrow peaks is discussed in the following chapter). For this reason, it would be appropriate to use the lanthanide-based upconverters in some studies defined at certain wavelengths. Although there is one study conceptually proposed on lanthanide-based upconverters [42], any experimental study that determines the performance of lanthanide-based upconverters in detectors does not exist.

There are some commercially available infrared sensing cards utilized to determine the location and size of the beam. These cards generally include the lanthanide-based photosensitive area.

1.1.1.4 Thermal Sensors

Conventional temperature sensors' disadvantages, such as sensitivity to electromagnetic influences and slow response, limit their applications [43], [44]. Therefore, studies on the improvement of optic-based temperature sensors have received great attention. Optic-based temperature sensors exhibit not only immunity to electromagnetic fields and fast response, but also they are cheap, stable, and portable [44], [45].

The sensing mechanism of optic-based temperature sensors is generally based on measuring the blackbody radiation or the physical disturbance of fiber due to temperature variation. A new technique based on the temperature-dependent photoluminescence of lanthanide ions has received considerable interest in recent years [43]. Unlike some methods, measuring photoluminescence of lanthanide ions provides non-contact thermal monitoring in a wide range of scales [46], [47].

Using lanthanide-based sensors, temperature is measured by taking the fluorescence intensity ratios (FIR) of two upconversion emission peaks [43], [48]. It shows that lanthanide ions have temperature-dependent upconversion due to thermally coupled levels present in the lanthanides, such as Thulium (Tm) [49], Holmium (Ho) [50], and Erbium (Er) [46], [51]. The most investigated active ion is Er for the thermal sensor, and Manzani et al. [52] have obtained one of the highest temperature sensitivities (0.0089 K^{-1} at 473 K) for Er^{3+}/Yb^{3+} co-doped tellurite glasses. As already mentioned, these sensors work in a wide-range temperature scale. For example, Dovile et al. [49] achieved the highest sensitivity at 175 K.

1.1.1.5 3D Volumetric Displays

Volumetric displays create a 3D vision with 360 degree viewing angles, unlike illusion based popular 3D TVs. Downing et al. [53] were the first in demonstrating the upconversion-based volumetric display in rare-earth-doped heavy metal fluoride glass. They excited each voxel (the equivalent of a pixel in 3D space) by using a special setup includes laser diodes and a mechanical scanning system. They used different laser combinations and different glass compositions or doping concentrations to create different colors. For example, 0.5% Er^{3+} doped ZBLAN (ZrF_4-BaF_2-LaF_3-AlF_3-NaF) creates green color when excited with 1014 nm and 840 nm lasers at the same time. Since then, new methods and materials have been improved [54]–[56]. In a recent study, Deng et al. [9] introduced core-shell upconversion nanocrystals, which achieve a dynamic emission along to all color

spectra. Moreover, they modulated the emission color by changing the pulse width of excitation laser beams.

1.2 Thesis Outline

The second chapter of the thesis describes the background and theory behind the upconversion from lanthanide ions. It starts with explaining lanthanides and their optical properties. Then, the operation principle of upconversion and material requirements are investigated. The section ends with a literature review on ytterbium-erbium silicate thin films.

The third section provides a summary of the experimental methods employed in this study to fabricate and characterize the films. The methods include rf magnetron sputtering and photoluminescence.

The fourth section starts with the deposition parameters of the films. Then, the structural and luminescence properties of the samples are given in the section.

CHAPTER 2

BACKGROUND AND THEORY

2.1 Lanthanides and Optical Properties

2.1.1 Energy Levels of Lanthanide Elements

Lanthanides (Ln) comprises 15 elements from lanthanum to lutetium with atomic numbers 57-71. The most stable oxidation state of lanthanides is +3 and trivalent lanthanides (Ln^{3+}) have a general electronic configuration [Xe] $4f^N$ (N = 0(La)-14(Lu)). However, +2 and +4 states of lanthanides are also known [57].

Coulombic interaction between 4f electron(s) and the positively charged nucleus splits the 4f level into a set of manifolds, also called meta-stable energy levels. Due to the shielding of the 4f shell by filled $5s^2$, $5p^6$ subshells, positions of these manifolds are independent of the host material, which results sharp and narrow f–f transition bands covering from the ultraviolet to near-infrared ranges (0.3-2.2 μm) [58], [59]. Since these transitions are Laporte-forbidden (parity selection rule), the lifetimes of the excited states are long (up to ~15 ms for Er [60]), and absorption coefficients are very low. As a result of the induced crystal field by host material, 5d states mix with 4f states, the symmetry of Ln ion gets disturbed resulting in weakening in the parity selection rule, finally, relaxations occur [57]–[60].

As mentioned before, the most significant perturbation occurs due to the Coulombic interactions in lanthanides. The second-largest splitting caused by the spin-orbit interactions refers to the coupling of spin and orbital angular momentum. Due to the well-screened 4f level by the filled 5s and 5p shells, the spin-orbit coupling effect is more prominent than the crystal-field effect [61]. Finally, energy levels of a

lanthanide ion placed in a crystal field split apart in energy, the so-called Stark splitting. All splitting mechanisms and corresponding energy differences between sublevels are graphically summarized in Figure 2.1.

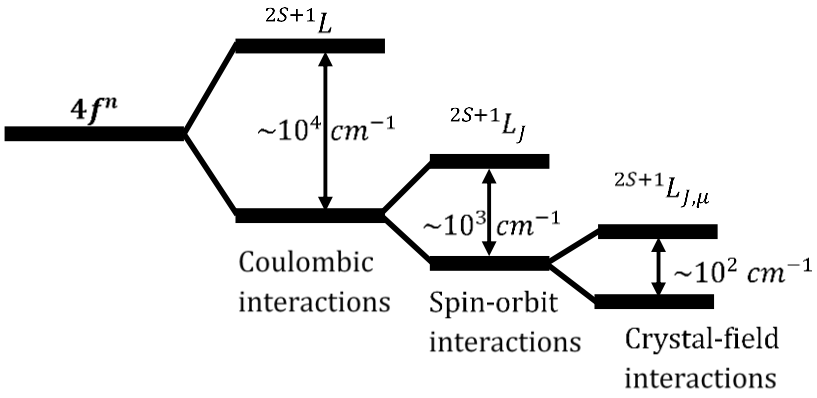

Figure 2.1. Schematic representation of the splitting of the $4f^N$ configuration due to atomic and crystal field interactions, and the interactions' order of magnitude of effects

The energy levels created by Coulombic relations were determined by Dieke et al. [62] for all trivalent lanthanide ions. They demonstrated these data in the energy diagram known as Dieke diagram. Since then, computational and experimental works that are compatible with Dieke diagram have been employed to determine the exact position of these levels [63]. Figure 2.2 illustrates the calculated 4f energy levels of some trivalent Ln ions by using Dodson and Zia method [64].

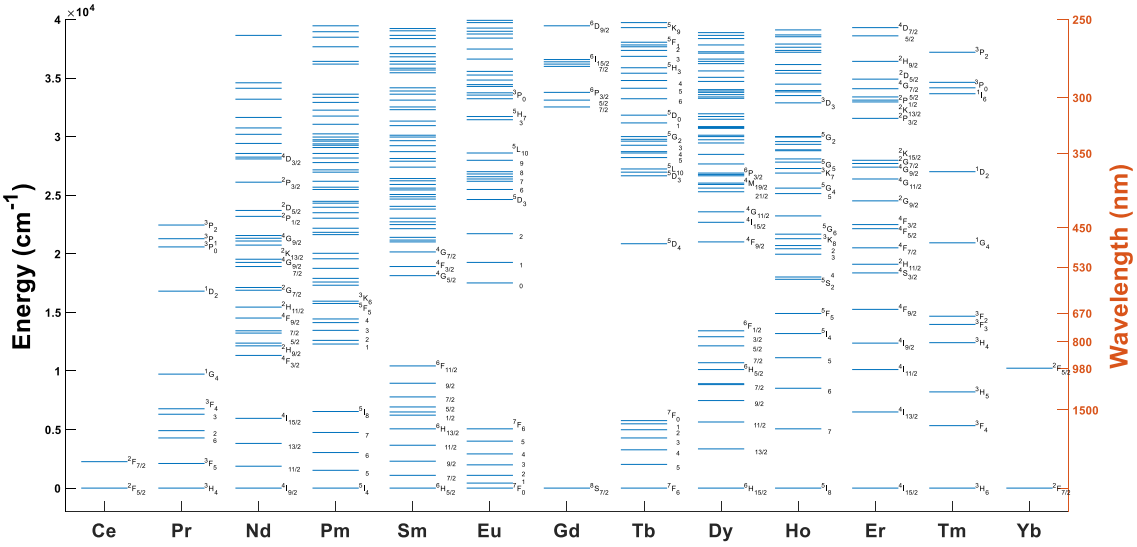

Figure 2.2. Dieke diagram (energy levels of some trivalent lanthanide ions) calculated using the Dodson and Zia method [64]

2.2 Material Requirements for Upconversion

Upconversion can be observed in various material types with different working principles, such as triplet-triplet annihilation (in organic dyes), two-step absorption (in quantum nanocrystals), and sequential absorption (in lanthanides). Furthermore, there are other anti-Stokes processes, including second harmonic generation and multiphoton absorption, in which the combination of low energy photons results in the emission of a photon with higher energy. While absorption and emission are carried out through the virtual states in these processes, upconversion emission takes place by using real energy states [65]–[67].

Since the goal of our work is to obtain upconversion from Ln ions in an inorganic host (ytterbium-erbium disilicates), upconversion performance of lanthanides and inorganic host materials are discussed in this chapter.

2.2.1 Lanthanides as an Activator

As already mentioned, excited states of lanthanides have long lifetimes. The long lifetime allows sequential excitations in excited states of a single Ln ion, and energy transfers between two or more Ln ions. These two mechanisms make lanthanides the best candidate for upconversion active ion. However, the energy levels of most lanthanides are not suitable for upconversion. As shown in Figure 2.2, ytterbium and cerium have just one excited state, and gadolinium does not have any state up to 32000 cm^{-1}, corresponding to 312 nm. In addition, other ions (except for erbium, thulium, and holmium) have many excited states below useful energies for the current applications of upconversion. Moreover, to achieve efficient upconversion emission, all energy spacings between metastable states of lanthanides must be similar, yet most of them have large differences. For example, in dysprosium ion, the energy gap between the first excited state and the ground state is much higher than the difference between the second and first states. Since the excitation photon energy must be higher than the first energy gap, the incident photon energy would be much higher than the second gap. Eventually, the excess energy is lost by thermalization.

Erbium, thulium, and holmium are the most investigated ions as an upconversion material thanks to their ladder-like energy level structure, and are called activator ions; that is, the ions which combine the low energy photons.

2.2.2 Upconversion Host Materials

In addition to the selection of lanthanide ions (activator and sensitizer), choosing the host material (i.e., surrounding environment of the ion) is crucial in terms of upconversion efficiency and emission profile because the host determines not only the distance between the dopant ions but also the crystal field that affects the ions. An efficient upconverter material requires a host matrix with low phonon energy and good lattice matching to the lanthanides [32], [66].

Lanthanides share chemical similarities, which are due to the fact that they have a similar ionic radius, and their most stable oxidation state is the same. Therefore, inorganic compounds containing lanthanide ions are the best candidate for host matrix [68], [69]. Moreover, inorganic compounds containing cations such as Na^{+}, Ca^{2+}, Sr^{2+}, and Ba^{2+} are frequently studied as host matrix, because they also have similar ionic size [17], [61]. Indeed, Na^{+} based compounds are one of the most efficient upconversion host matrices [70], [71]. In addition to all these compounds, wide bandgap semiconductors, such as GaN, AlN, InN (III-Nitrides), ZnS have been employed as upconversion host materials [72]. However, to the best of our knowledge, any remarkable upconversion efficiency could not be obtained by using these materials. Besides the above-mentioned materials, lanthanide-based compounds, such as silicates and molybdates [73], [74] have attracted considerable attention since they overcome solid solubility phenomena that causes segregation or clustering of lanthanide ions. However, because of their high phonon energy, the studies generally examine downconversion properties of the compounds to uncover their waveguide potential rather than upconversion.

The second requirement for ideal host material is that it should have low phonon energies. Here, it is important to describe the relation between phonon energy and the radiative emission from a 4f level. If less than six phonons are required to bridge the energy gap, the excitation decays non-radiatively (the transition is completed with multiphonon relaxation), resulting in lower upconversion efficiency. The highest typical phonon energies for different types of crystals are tabulated in Table 2.1 [75]. As shown in the table, heavy halides have the lowest phonon energies. On the other hand, not only do they exhibit poor thermal, chemical, and mechanical properties, but they are also hygroscopic, complicating synthesis (compared to oxides) [76], [77]. Therefore, the investigation of oxide materials is continuing, despite their high phonon energy. For example, Gd_2O_2S is one of the most promising host materials, and it exhibits good thermal, chemical, and mechanical properties [28].

Normally same parity transitions are forbidden in crystals with high symmetry, where parity selection rule has to be obeyed. The last requirement for ideal host material is high emission cross-section, which is fulfilled with low crystal field symmetry. This effect is prominent in the $NaYF_4$ that is one of the most examined host matrices. While the distribution of Na^+ and Y^{3+} cations are random in the cubic structure of $NaYF_4$, these cations symmetrically occupy the lattice sites in hexagonal NaY_4 [71], preserving the cubic structure. However, the upconversion efficiency of $NaYF_4$ decreases one order of magnitude during phase change to other types of cubic structures [70].

Table 2.1 Maximum phonon energies of common inorganic hosts

	Max. phonon energies (cm^{-1})
Oxide	600
Fluoride	355
Chloride	260
Bromide	172
Iodide	144

2.2.3 Upconversion Loss Mechanisms

Multiphonon relaxation, concentration quenching, and cross-relaxation are three main loss mechanisms for upconversion. While multiphonon relaxation and concentration quenching are relaxation mechanisms, cross-relaxation is an energy transfer mechanism accompanied by radiative emission. These loss mechanisms are detailed in this section.

2.2.3.1 Multiphonon Relaxation

The interaction between lanthanide energy states and host matrix lattice vibrations results in emission of multiple phonons. In other words, the excitation energy is

converted into heat, meaning optical losses. The multiphonon decay rate was modeled by Riseberg-Moos [78] and summarized by the following equation:

$$W_{MPR} = W_0 * \left\{1 - \exp\left(\frac{\hbar w}{kT}\right)\right\}^{-\Delta E/\hbar w} \quad (2.1)$$

where W_0 is the spontaneous decay rate at 0 K, $\hbar w$ is the maximum phonon energy, ΔE is the energy gap in which the relaxation occurred. The power of the second term is equal to the number of phonons required to bridge the gap. It appears from the equation that the multiphonon decay rate increases with raising phonon energy. Because the energy of the phonons depends on the mass of lattice ions and binding energies between them, the efficiency can be increased by choosing a host lattice with low energy phonon, as already discussed in the previous section.

2.2.3.2 Quenching Centers

The excitation relocates between lanthanide ions in the lattice, the so-called energy migration. Due to the long lifetimes of lanthanide energy levels, the energy transition rate is high in lanthanide-doped systems. The energy transfer is not a loss mechanism, because it does not affect total excitation. However, when transferred excitations are trapped by the quenching centers (e.g., impurities, defects), the excitations are non-radiatively lost. Grain boundary sites, oxygen vacancies, and hydroxyl (OH^-) groups (Especially for erbium due to the fact that stretch mode of their second harmonic is resonant with $4I_{15/2} \rightarrow 4I_{13/2}$ transition) are quenching centers [79]. To decrease the quenching loss, the average distance between the ions is increased, due to the migration rate being inversely proportional to distance, as shown in Equation 2.2. The most common way to increase distance is by diluting activators with yttrium and ytterbium ions.

The energy migration rate is [80]:

$$W_{qr} = 8\pi * C_{em} * N_{Ln} * N_q \quad (2.2)$$

where W_{qr} is quenching rate caused by energy migration, C_{em} is energy migration constant, N_{Ln} is the density of lanthanides, N_q is the concentration of the quenching centers.

2.2.3.3 Cross-Relaxation

Cross-relaxation (CR), which appears between two identical ions, is an energy transfer mechanism. The transfer occurs initially between an upconverted ion (at second energy level) and another ion in the ground state, the upconverted ion transfers a part of its energy to the other ion, and this process results in both ions to be in the intermediate state, illustrated in Figure 2.3. Although total energy is conserved whereby the lost energy for the first ion is equal to the excitation energy of the second ion, the cross-relaxation is a loss mechanism for upconversion. The average distance between identical ions should be extended to decrease the cross-relaxation rate, just like the decreasing effect of quenching centers.

2.3 Upconversion Mechanisms

The upconversion phenomenon in a lanthanide ion for a solid-state infrared quantum counter was first suggested by Bloembergen in 1959 [1]. Until 1966, it was considered that all energy transfer processes occurred between rare-earth ions, which one of them was in its ground state. In other words, the absolute energy is constant. Auzel proposed to consider the case of energy transfer between ions in excited states [81]. That is, he explained how upconversion is formed via energy transfer. The most common upconversion mechanisms are Excited state absorption, Energy transfer upconversion (the most efficient upconversion mechanism [16]), and Cross sensitization upconversion.

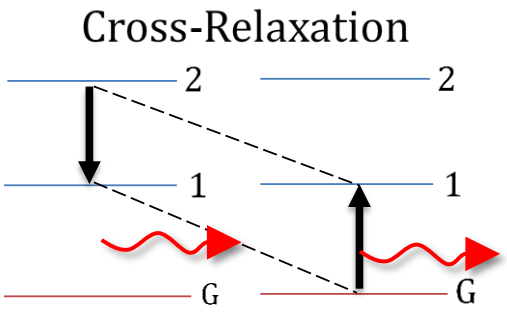

Figure 2.3. Schematic representation of cross relaxation. The energy transfer between the two ions populates intermediate levels of both ions. Photons are emitted when both intermediate levels decay to ground state (represented by the curved red lines).

2.3.1 Excited State Absorption

Excited State Absorption (ESA) is the fundamental mechanism of upconversion processes. Ladder-like energy states sequentially absorb incident photons. Photon absorption by an ion in the ground state is called Ground State Absorption (GSA), and photon absorption by an ion in the excited state (previously GSA absorbed) is called excited state absorption. Since there is no limitation for the number of absorptions, absorptions may continue to happen until a cross-relaxation or emission of a photon with higher energy occur. Figure 2.4 depicts a ground state absorption followed by excited state absorption in a three-level system.

2.3.2 Energy Transfer Upconversion

The Energy Transfer Upconversion (ETU) process utilizes two neighboring ions, which can be identical or different. They are known as sensitizer and activator. The sensitizer is initially in the excited state, and it transfers its energy to the activator; then, the transferred energy excites the activator to its upper level in energy. The activator can be in its ground state or excited just before transition. If excited, the upconversion occurs when ETU is accompanied by a radiative relaxation. Figure 2.5

illustrates that the sensitizer sequentially absorbs two photons and transfers them to the activator, the activator, with a three-level system, then emits a higher energy photon relative to incident ones.

The most popular sensitizer is ytterbium since its energy level structure is suitable for common activators and its absorption cross-section is large (e.g., one order of magnitude bigger than erbium at 980 nm) [82]. Wang et al. [83] compared photoluminescence efficiencies of two samples, which are only erbium-doped and erbium-ytterbium co-doped. They observed 200 times enhancement in both ytterbium and erbium-doped sample.

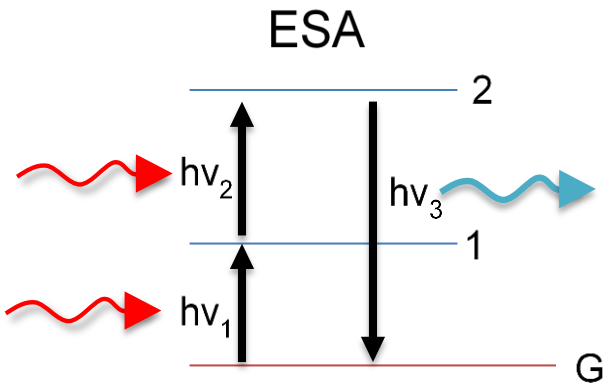

Figure 2.4. Schematic representation of Excited State Absorption (ESA). Sequential absorption of incident photons results in the population of a higher excited state. The curved red and turquoise lines represent absorbed and emitted photons, respectively.

2.3.3 Cooperative Sensitization Upconversion

Cooperative Sensitization Upconversion (CSU) is similar to ETU in that both upconversion processes use the transfer of energy from one ion to another. The difference between these mechanisms is that ETU occurs between two ions, while CSU occurs between three ions. Both initially excited sensitizers transfer their energy to a third ion (emitter), which then radiatively decays to its ground state. Since the energy transitions need to be at the same time, the probability of occurrence of the process is very low [65]. The process demonstrated in Figure 2.6.

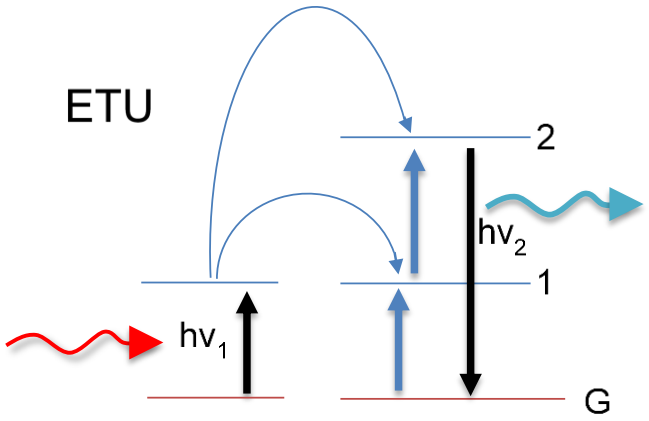

Figure 2.5. Schematic representation of Energy Transfer Upconversion (ETU). Energy transfer to the excited activator results in the population of a higher excited state. The curved red, turquoise and blue lines represent absorbed, emitted photons and energy transitions, respectively.

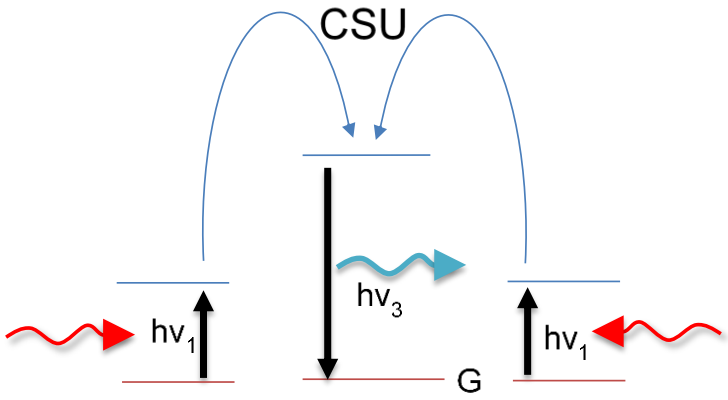

Figure 2.6. Schematic representation of Cooperative Sensitization Upconversion (CSU). Energy transfer from initially excited sensitizer ions to the third ion results in the population of a higher excited state. The curved red and turquoise lines represent absorbed and emitted photons, respectively.

2.4 Upconversion by Erbium Silicates

In this work, we exhibit achieved results on NIR to NIR upconversion from $Er_xYb_{2-x}Si_2O_7$ films, and this section summarizes some of the prior works on erbium silicate films. Erbium silicate compounds were first fabricated by Isshiki et al. [84] in 2004.

They deposited the silicates by coating $ErCl_3$/ethanol solution on silicon substrate followed by oxidation and annealing, observing an emission at 1530 nm with a peak linewidth just ~7 nm. Since then, erbium silicate compounds have attracted great interest because they contain a high density of erbium (emitter). This interest has been mainly dedicated to developing an efficient light source and waveguide at ~1550 nm, which corresponds to the minimum loss of silica optical fibers [73], [85], [86]. Numerous methods are utilized for fabricating erbium silicates, such as laser ablation, metal-organic beam epitaxy, sputtering, sol-gel methods, and the reaction of $ErCl_3$ with silicon. Sputtering is a complementary metal oxide semiconductor (CMOS) compatible deposition technique, allowing the deposition of uniform films, making it the most widely used fabrication method to produce erbium silicates [73], [74], [87], [88].

Priolo's group has made great efforts to optimize the fabrication of erbium silicate thin films in terms of substrate and annealing (method, temperature, and ambient gas) [73], [85]. Moreover, they demonstrated that the small distance between erbium ions yields a high energy transfer rate, which increases the effect of material defects and quenching of luminescence [86]. In 2010, three groups suggested diluting erbium ions with Ytterbium (Yb) or Yttrium (Y) ions to decrease energy migrations by increasing the distance [74], [87], [89]. They optimized luminescence properties by changing erbium and diluting ion concentration. Wang et al. [90] enhanced luminescence of around 30 times for yttrium-erbium silicate compared to pure erbium silicate, and they demonstrated 200 times enhancement for ytterbium-erbium silicate [83]. The difference comes from the fact that the absorption cross-section of ytterbium ions is an order of magnitude larger than erbium ions at 980 nm [82]. In addition to the optimization of thin films, the same group demonstrated upconversion luminescence from a millimeter size erbium-ytterbium waveguide [91]. However, they could not observe any upconversion feature from the thin film form of the same compound [92]. To the best of our knowledge, an upconversion spectrum from silicate thin films was indicated in only one study, which was published by Vanhoutte et al. [87]. The film thickness was 450 nm in that study.

As previously mentioned, the focus of erbium silicate research is to fabricate an advanced waveguide at the communication band. The most enhanced erbium silicate waveguide was produced by Sun et al. [93], in 2017. Their single-crystal erbium chloride silicate nanowire has achieved a high unit net gain of 124.5 dB/cm at 1532 nm.

CHAPTER 3

EXPERIMENTAL METHODS

This chapter gives a brief overview about the techniques used for thin film deposition and for their structural and optical characterization. In this work, the upconverter thin films were deposited using reactive and direct rf magnetron sputtering at the same time. Therefore, this chapter begins with explaining both the sputtering processes, and it provides optimization methods for the estimation of the fabrication parameters. Finally, the setup of photoluminescence and an enhanced model for frequency-domain lifetime measurements are reviewed. Although Scanning Electron Microscope (SEM), X-ray diffraction (XRD), Ellipsometry, Raman were also performed for structural, chemical, and optical characterization, we did not discuss these methods because no novelty was added to these methods, nor did we do their optimization.

3.1 Deposition of Films

3.1.1 Sputtering

Sputtering is a physical thin film deposition process where energetic ions knock off surface atoms or molecules of the source material (or target), after which the ejected particles condense on the substrate. To obtain highly pure thin films, a clean environment with only deposition materials is required. Therefore, sputter deposition occurs in an isolated chamber from the atmosphere. In addition to the chamber, the sputtering system consists of vacuum pumps, gas lines, power generators. Sputtering deposition begins with evacuating the initial gas from the chamber. Then, the chamber is backfilled with inert gas, which is generally argon. When a negative bias is applied to the target, the target behaves as the cathode, and the chamber as the

anode. Consequently, free electrons are created, and they accelerate away from the target because the ionization potential of gases is typically higher than the work functions of solids. As a result of collisions between free electrons and argon gas molecules, positively charged gas ions are created. These ions are accelerated towards the target due to the electric field, and the sputtering event occurs. Figure 3.1 depicts the sputtering deposition process. Figure 3.2.a shows a photograph of the sputtering system used to deposit the films studied in this thesis in this thesis, and Figure 3.2.b is a scaled schematic of the chamber.

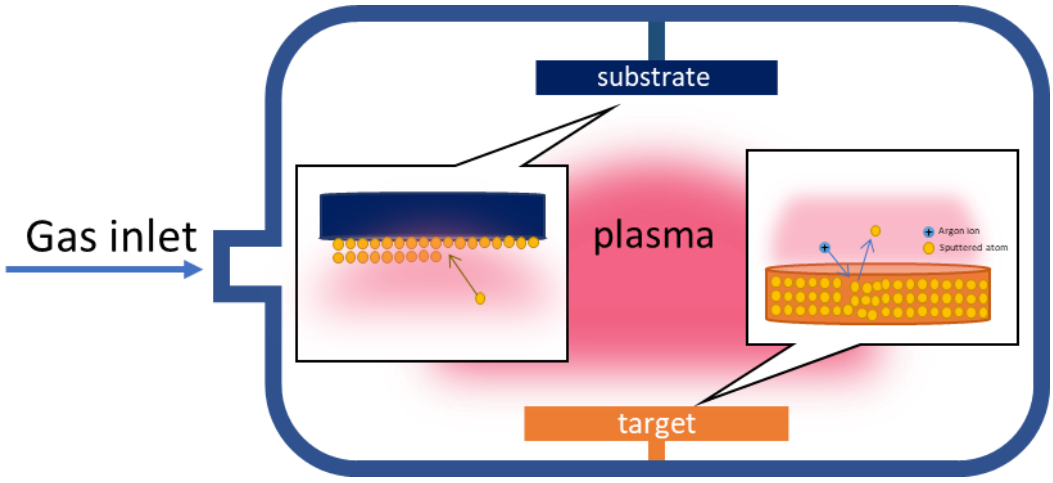

Figure 3.1. Schematic representation of the sputtering process. Insets demonstrate the ejection of atoms from the surface of the target material and condensation of them on the substrate.

The most popular sputtering modes, dc and rf; types of target power supply. In the former technique, the sputtering target and the substrate are always cathode and anode, respectively. Sputtering insulators by direct current is not possible because of surface charging, which repels the energetic argon ions.

Davidse and Maissel [94] have proposed using an rf source to prevent a charge build upon the target. Because of the high mobility of electrons compared to ions, during positive polarity, many more electrons will reach the insulator surface than the charge collected during the negative polarity, and the target surface will remain negative. The permanent negative surface repels the electrons and creates ion rich

space in the vicinity of the target. It allows high deposition rates and prevents the polarized charge related problems such as arcing phenomena and disappearing anode [95].

In order to trap ejected electrons, close to the surface of the sputter target, a magnetic field is created with the help of a magnet placed into the magnetron. The high density of electrons increases the probability of electron-argon collisions and thus ionization of argon ions increases in the vicinity of the target, which results in an increase in deposition rate. Indeed, the magnetic field does not affect sputtered atoms because they are mostly neutral. This thin film deposition method is called magnetron sputtering. The biggest disadvantage of this method is that the target surface erodes in the target regions where the plasma density is highest, and it causes the poor target utilization.

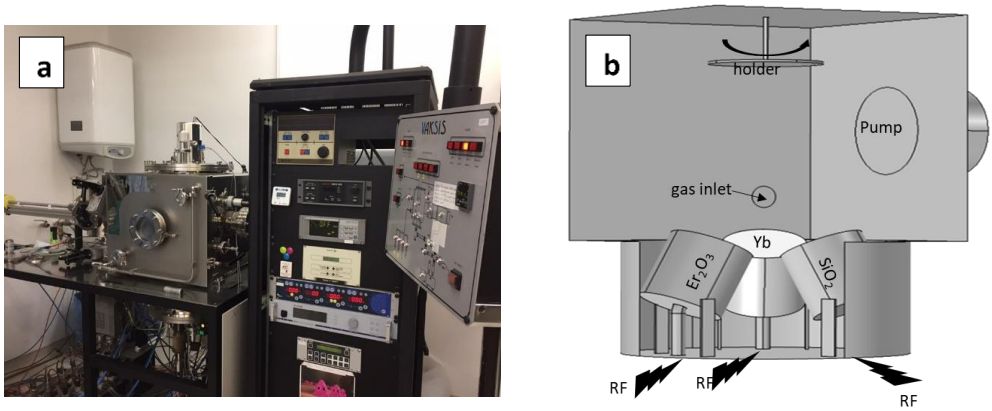

Figure 3.2. (a) A picture of Varian rf magnetron sputter system and (b) scaled schematic of the chamber used for this work

3.1.1.1 Reactive Sputtering

Reactive sputtering refers to the sputtering of metal or metallic target in the presence of reactive gas (typically, oxygen or nitrogen). The deposited film forms a compound of the target and the reactive gas. Although deposition of compounds is possible with compound targets, which is called direct sputtering, reactive sputtering allows

adjustment of the chemical composition of the film and achieving high deposition rates.

Since the reaction between the metal atom and the gas is highly exothermic, removing the excess energy requires a third partner. These three-body collisions are rare due to low sputtering pressure, the reaction only occurs on target or exposed surfaces [96]. In other words, the desired compound grows in two ways; first, the reaction of the target with the gas to form a compound then later deposited onto the chamber walls (including substrate) or reaction of the sputtered atom on chamber walls with the gas after deposition. If the gas flow is continuously increased, the whole surface of the target turns into a compound form, commonly known as target poisoning. This leads to a sudden decrease in the sputtering rate with a hysteresis feature. Figure 3.3 illustrates the hysteresis feature of the reactive sputtering process. The curve is obtained by using Berg's model [97]. As shown in the figure, the compound rate on the target increases with a rising flow rate up to a critical value and the target is abruptly poisoned. The flow rate must be decreased to another critical point to get rid of the poisoning.

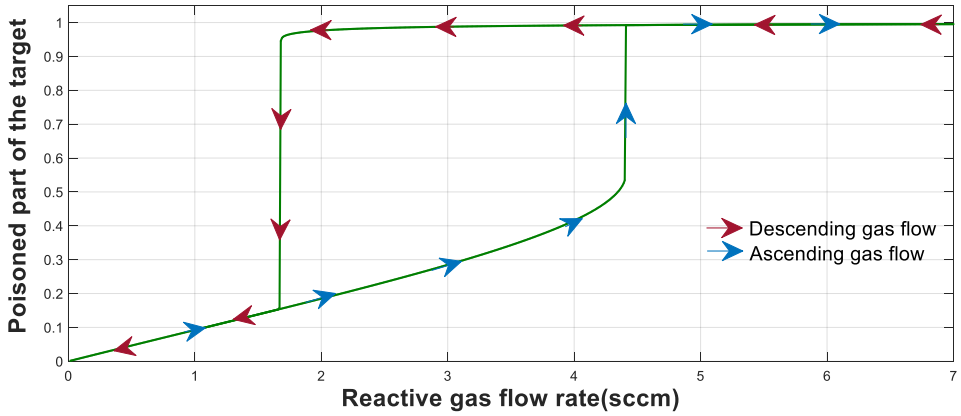

Figure 3.3. The fraction of the formed compound as a result of interaction between reactive gas and the target as a function of the flow of reactive gas

In this work, we have fabricated erbium-ytterbium silicates by using erbium oxide and silicon dioxide compound targets and a metal ytterbium target. That is, we used the reactive sputtering method to form ytterbium oxide. Because of very high

sputtering yield (the sputtering yields of Ytterbium, Aluminum and Silicon are shown in Figure 3.4) and easy oxidation of the ytterbium target, the ytterbium target was not stable during depositions and it was poisoning after a while. Its pictures, at the beginning of deposition and 15 minutes later, are given in Figure 3.5. The poisoning of the target is clearly seen in Figure 3.5.b because the change in plasma color indicates that the increasing fraction of the compound on the target surface decreases the electron density and the average kinetic energy of the free electrons [98]. Due to the chemical instability of the target surface, we controlled the deposition process to enhance the stoichiometry of the films. Since the resistivity of target changes as a function of the compound-metal ratio on the target surface, the poisoning of the target can be followed by monitoring the cathode voltage when constant power is applied. The change in cathode voltage with the reactive gas flow is given in Figure 3.6. Here, the cathode voltage increases with the reactive gas flow rate, and the voltage rises sharply when the target is poisoned. Also, the cathode voltage as a function of the decreasing flow rate is shown in Figure 3.6. To enhance film quality, the process was restarted each time it approached poisoning mode by monitoring the bias voltage.

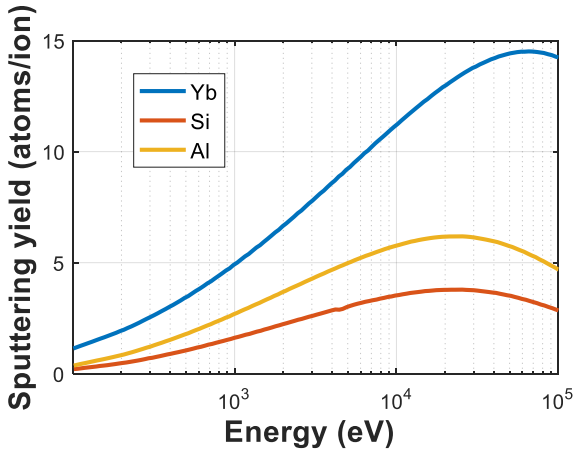

Figure 3.4. Sputtering yields of Ytterbium, Aluminum and Silicon as a function of energy of sputtering gas (reproduced from data obtained by personal communication with www.npl.co.uk)

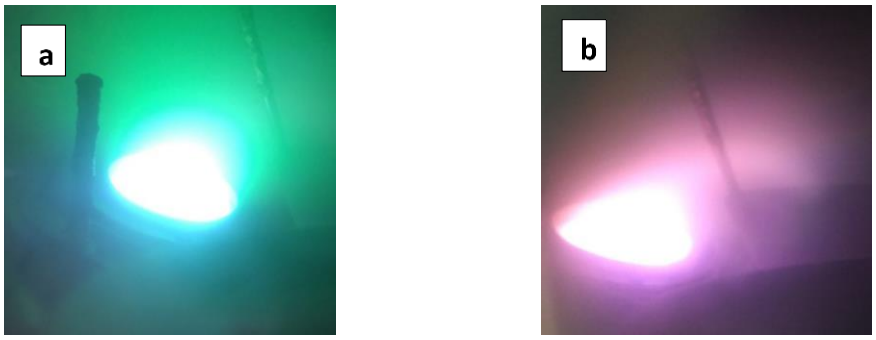

Figure 3.5. The pictures of the ytterbium target taken (a) at the start of the deposition (b) after 15 minutes. The target is visibly poisoned in (b).

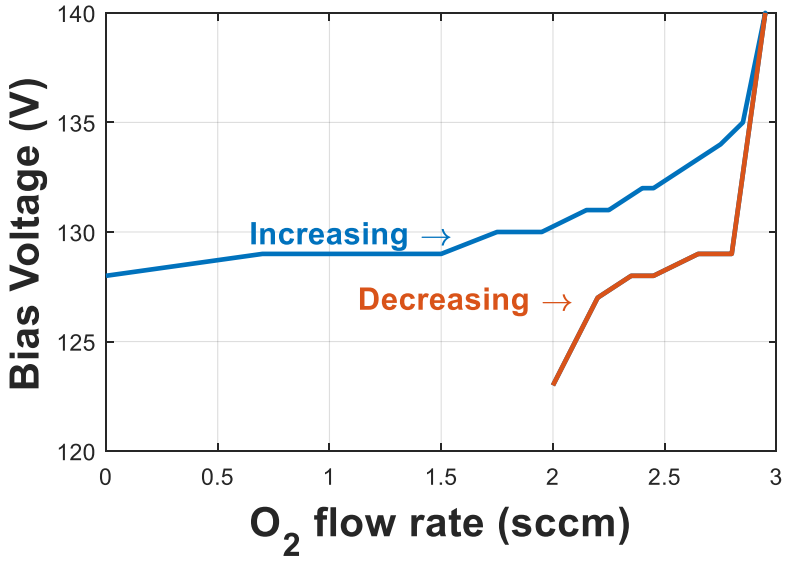

Figure 3.6. The change in cathode voltage with the reactive gas flow.

3.1.1.2 Direct Sputtering

Whereas ytterbium oxides were formed by the reaction of the sputtered metal and oxygen gas, the sputtering of oxide targets (erbium oxide and silicon dioxide) was directly done. Deposition rates required to obtain nearly stoichiometric silicate films are determined using the following chemical formula and concentrations of compounds.

$$xEr_2O_3 + 2 * (2 - x)Yb + 4SiO_2 + O_2(gas) \rightarrow 2Er_xYb_{2-x}Si_2O_7$$

The concentration of a compound is calculated with following expression:

$$r(Concentration[in\ \#atoms\ per\ cm^3\ ]) = \frac{N_A\ \rho}{M} \tag{3.1}$$

where N_A is the Avogadro number ($6.022 * 10^{23}\ mol^{-1}$), ρ is the density (in g/cm^3), M is the molar mass (in g) . Table 3.1 demonstrates these properties of the compounds.

Table 3.1 Molar mass, density, and concentration properties of the used sputtering targets

	Molar Mass *(g)*	*Density* *(g/cm^3)*	*Concentration* *$(\#atoms\ /\ cm^3)$*
Er_2O_3	382.56	8.64	$1.36*10^{22}$
Yb_2O_3	394.08	9.17	$1.40*10^{22}$
SiO_2	60.08	2.65	$2.65*10^{22}$

The relations between deposition rates of the targets are calculated by using their concentrations and coefficients (the number of molecules involved in the silicate) to deposit a specific stoichiometry, and they can be formulated as the following expressions:

$$\frac{[Er_2O_3]}{[SiO_2]} = \frac{x}{4} * \frac{r(SiO_2)}{r(Er_2O_3)} = 0.49 * x \tag{3.2}$$

$$\frac{[Yb_2O_3]}{[SiO_2]} = \frac{2-x}{4} * \frac{r(SiO_2)}{r(Yb_2O_3)} = 0.47 * (2-x) \tag{3.3}$$

Figures 3.7.a and 3.7.b demonstrate deposition rates of erbium oxide and silicon dioxide targets as a function of applied power, respectively. Furthermore, a first-order curve was fitted to determine the intermediate values. Since the deposition rates of compound targets can be easily adjusted, the deposition rate of ytterbium was kept constant for all depositions.

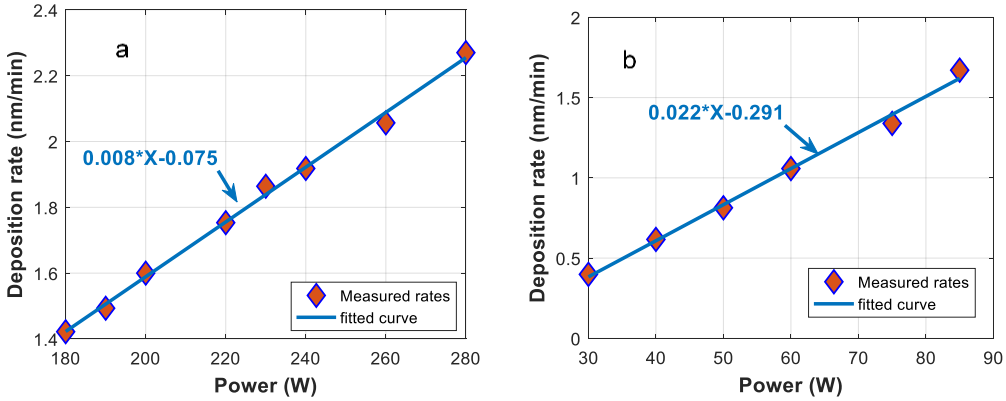

Figure 3.7. Deposition rates of (a) silicon dioxide and (b) erbium oxide targets as a function of applied power

3.2 Photoluminescence and Lifetime Measurements

3.2.1 Measurement Setup

In photoluminescence (PL) spectroscopy, the intensity of emitted light from a sample, under excitation, is measured as a function of wavelength. Since we are interested in upconversion or downconversion emissions of our samples, we employed two light sources, operating at 980 nm for downconversion and 1550 nm for upconversion.

PL spectra of our samples were analyzed using a monochromator and a photodiode (Silicon for upconversion, InGaAs for downconversion measurements), connected to a lock-in amplifier. The samples were excited with one of the lasers modulated at 60 Hz by TTL out of the lock-in amplifier. The PL emitted light is collected, then focused into the monochromator by two lenses. A schematic of our PL experiment setup is given in Figure 3.8. Measuring the PL spectrum of lanthanides requires intense excitation source and an advanced PL system with both a sensitive detector and a well-aligned optical setup due to low absorption and emission cross-sections of lanthanides. Unfortunately, we did not have a sensitive detector, so measuring visible upconversion was not possible. This is not a huge problem because we know

that the visible upconversion of our samples is very low due to the high phonon energy of our samples.

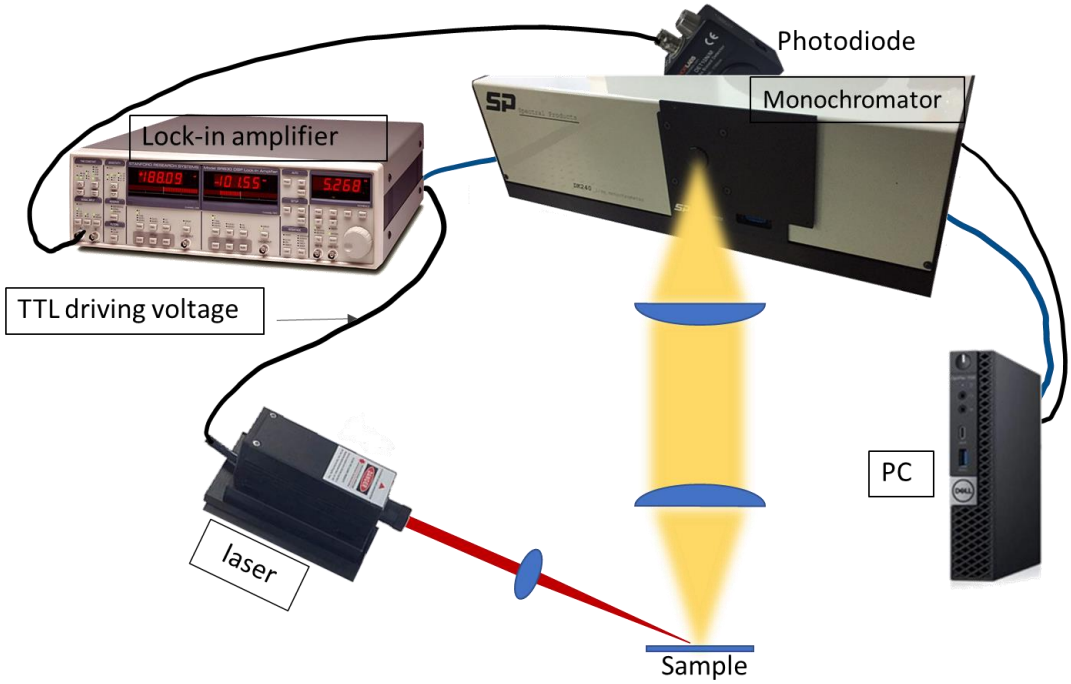

Figure 3.8. Schematic of PL setup

3.2.2 Measuring PL Lifetime

An excited sample emits photons with a decay time, that is called lifetime. The lifetime of a sample can be measured in the time domain or frequency domain. In time domain methods, the sample is illuminated with a train of light pulses and emission is detected with a time-resolved spectrometer. The decay time is determined from the slope of the natural logarithm of the intensity (Figure 3.9.a). On the other hand, frequency domain methods do not require transient excitation and time-resolved detection. In frequency domain methods, the sample is excited generally with a sinus wave modulated light. The sample emits light at the same frequency and with a delay that depends on the lifetime of the sample. The decay time is calculated from the delay measured as a phase shift (φ) between excitation and emission (Figure 3.9.b). Since time domain methods need expensive, complex

equipment and time, they are not suitable for real-time applications. Therefore, frequency domain methods that allow measurements of nanosecond or faster lifetimes are preferred in real-time applications [99]–[101]. Indeed, comparative studies between time and frequency domain methods have shown that they perform equally [102]–[104]. In addition to all this, the frequency domain method allows measurement of the lifetime of samples with very low emission intensities since a lock-in amplifier can be employed.

Philip and Carlsson [104] theoretically investigated signal to noise performances of different frequency domain lifetime measurement methods. They demonstrated that sinus as an excitation waveform is not optimal, and that the use of square wave reduces the errors caused by scattered light, confirmed by similar recent studies [102], [103]. However, the detected signal was processed by taking its Fourier transform to decompose the signal into its sinus constituents in studies using square wave excitation [102], [105], [106], requiring time. The extra processing of the signal limits the real-time usability of the method. Whereas a real-time lifetime measurement method for square-wave excitation exists in the time domain and is known as rapid lifetime determination, there are no methods in the frequency domain, to our knowledge. Although there is a study that obtains lifetime under square wave excitation by lock-in amplifier, it can be considered that sinus wave excitation is used since the excitation frequency was kept high to prevent the detection of harmonics by the lock-in amplifier [107].

We extracted a relation between the quarter-phase shift output (Y) of the lock amplifier and the lifetime of a sample excited by a square wave; thus, we have paved the way for using square wave in frequency domain real-time applications. The lifetime measurements were performed with the same setup used to obtain the PL measurements shown in Figure 3.8. The extraction of the relation is as described below.

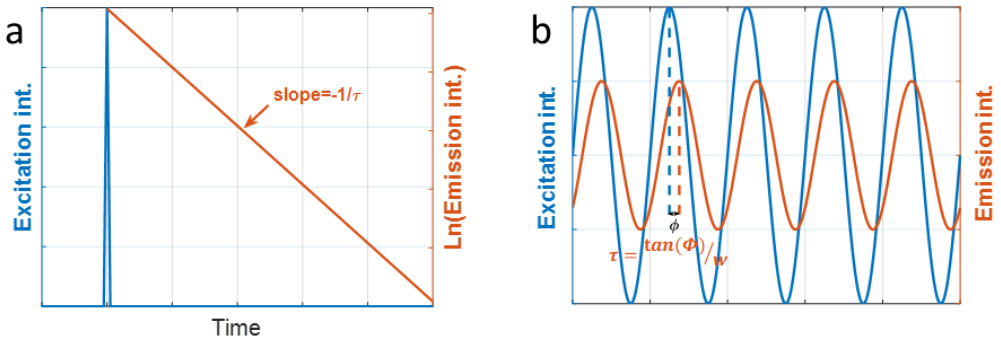

Figure 3.9. Excitation and emission waveforms (a) in time domain (b) in frequency domain

When a sample is illuminated by a light pulse at t=0, the excited population exponentially decays to the ground state. This exponential decay described as following:

$$I(t) = I_0 * e^{-\frac{t}{\tau}}, \qquad t > 0 \tag{3.4}$$

where t is the time, I_0 is the initial intensity and τ is the lifetime of the sample.

Because the excitation-emission mechanism behaves as a linear and time-invariant system in the absence of saturation and photobleaching, it can be characterized by its impulse response or its transfer function [108]. As is well known from system theory, the convolution of the impulse response and input function is equal to the output of the system. When the input is a square wave, the system's response becomes a piecewise function as follows:

$$Exc.\ Sig(t) \circledast I(t) = \begin{cases} I_0\left\{1 - e^{-\frac{t}{\tau}}\right\}, & 0 \le t \le \frac{T}{2} \\ I_0\left\{\left(e^{\frac{T}{2\tau}} - 1\right)e^{-\frac{t}{\tau}}\right\}, & \frac{T}{2} \le t \le T \end{cases} \tag{3.5}$$

where T is the period of excitation signal. This function is calculated assuming that the rising and decaying lifetimes are equal. However, they are inherently different, and this limits the practicality of our method. This problem is solved by using the

approach of matching the rising and decaying lifetimes, detailed below. The rate equation for the first excited level of an upconverter sample can be described as:

$$\frac{dN_1}{dt} = \sigma\Phi(N_{Er} - N_1) - \frac{N_1}{\tau_1} - C_{up}{N_1}^2 \tag{3.6}$$

The solution of the differential equation is much more complex than the solution of conventional emission function, the exponentially decaying function. Therefore, we solved the equation numerically by using MATLAB to investigate the upconversion coefficient and photon flux dependence of emission waveform. Figure 3.10 depicts that the rising and decaying lifetimes are equalized when the excitation photon flux or upconversion coefficient is low. In addition to the system response, we mathematically modeled the output of the lock-in amplifier shown schematically in Figure 3.11 to complete the relation between the lifetime and the output.

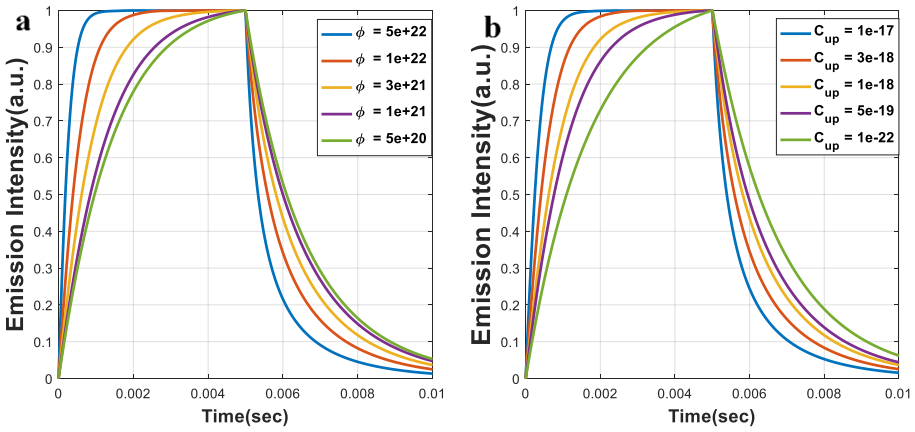

Figure 3.10. The dependence of emission waveform to (a) photon flux density and (b) upconversion coefficient

The mathematical model of the Y output is:

$$Y = mean\left(wave * \cos\left(wt + \theta_{ref}\right)\right) \tag{3.7}$$

where *wave* is the output signal of detector, w is modulation frequency of the excitation light and is referenced to the lock-in amplifier, θ_{ref} is the phase shift that can be introduced to the amplifier. The output of the low pass filter (Y output) is

equal to offset of the input signal. Therefore, the output can be found by integrating the product of the reference signal with the same frequency as the excitation signal and the piecewise function over one period. If we equalize the Y output of the locking amplifier to zero, the relation between lifetime and angle is derived as follows:

$$Y = C_0 \left[\int_0^{T/2} \left(1 - e^{-t/\tau}\right) \cos\left(wt + \theta_{ref}\right) dt + \int_{T/2}^{T} \left(e^{T/2\tau} - 1\right) e^{-t/\tau} \cos\left(wt + \theta_{ref}\right) dt \right] = 0 \tag{3.8}$$

where θ_{ref} is the reference phase shift.

$$\tan\left(\theta_{ref}\right) = \frac{-B\tau w}{2 + (\tau w)^2 * (2 - B)} \tag{3.9}$$

$$B = 2 - e^{-T/\tau} + e^{-T/2\tau} \tag{3.10}$$

To sum up, first, the reference phase shift is adjusted until the output is zero. Then, the lifetime is found by using Equations 3.9 and 3.10.

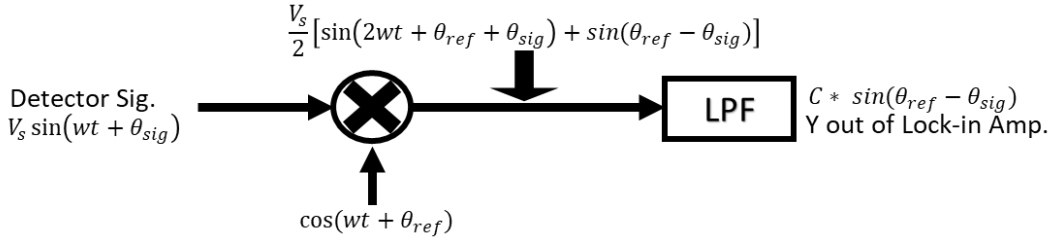

Figure 3.11. Block diagram of the lock-in amplifier. The incoming signal with a phase shift (θ_{sig}) is multiplied by reference signal with same frequency. The out is passed through a low pass filter.

CHAPTER 4

ERBIUM-YTTERBIUM SILICATES

4.1 Introduction

A compound of erbium, ytterbium, and silica was used as an upconversion material in this study, which aimed to produce stable materials with a high conversion rate. On account of its ideally suited energy levels for the upconversion of near-infrared light, erbium was employed as an activator. Ytterbium was used as a diluting and sensitizer ion due to its larger absorption and emission cross-sections and similar chemical properties with erbium. Silica was selected as the host matrix due to its stable thermal, chemical, and mechanical properties. Furthermore, to reduce the effect of silica's high phonon energy on upconversion efficiency, we worked with erbium-based compounds, thereby increasing the concentration of luminescence centers. Although there are different types of erbium silicates, we preferred disilicates for two reasons. First, the interfacial reactions with the substrate are limited in disilicates [109], [110]. Second, erbium disilicates exhibit the highest optical efficiency compared to other pure erbium silicates, and therefore only disilicates have been studied in most researches examining the luminescence of erbium-based silicates [73], [74], [85], [109].

This chapter covers the deposition and characterization of erbium-ytterbium disilicate samples. The chapter begins with the investigation of the deposition details. Then, Energy-dispersive X-ray spectroscopy (EDX) and ellipsometry results are taken into investigation. Next, the structural properties of the films are studied through XRD analysis. Then, the dependence of photoluminescence on excitation power and crystallography is examined. Finally, lifetime measurement results are presented.

4.2 Deposition

Erbium-Ytterbium silicate thin films were deposited using O_2 reactive rf-magnetron sputtering system and following the procedure described in Chapter 3. These films were produced in five different concentrations with various erbium-ytterbium ratios (i.e., x in $Er_xYb_{2-x}Si_2O_7$). As mentioned in the previous chapter, the deposition rate of the ytterbium target was kept constant, and the rates of the other targets were adjusted accordingly. The fabrication parameters of the films for varying x values are given in Table 4.1.

Although the desired thickness for each film was 200 nm, the produced thicknesses of films were thinner and variable, as seen from the ellipsometry results given in Figure 4.1. All films were thinner than expected, because raising the number of sputtered atoms increased collisions and reduced mean free path for the atoms, in the case of co-sputtering. The reason for the varying thickness of the films was that the ytterbium target did not remain stable during the process, as explained in chapter 3. The unstable deposition not only caused different thicknesses, but also caused disparity between achieved and desired erbium-ytterbium ratios, as shown in Figure 4.2.

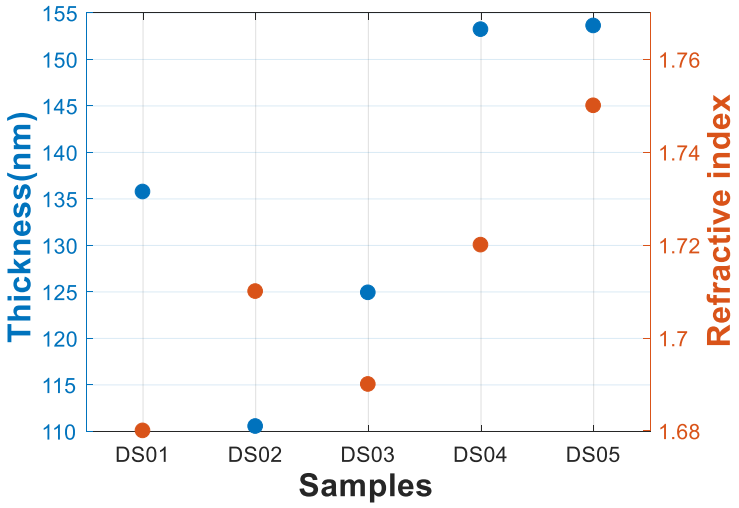

Figure 4.1. The refractive index and thickness of samples were extracted from the ellipsometry results by a Cauchy model

Table 4.1 Fabrication parameters of disilicate samples

Label	X	Er_2O_3		Yb_2O_3	SiO_2		Time (min)
		Rate (nm/min)	Power (W)	Rate (nm/min)	Rate (nm/min)	Power (W)	
DS01	0.2	0.15	20	1.5	1.75	230	60
DS02	0.4	0.20	25	1.5	2.00	260	55
DS03	0.6	0.30	30	1.5	2.28	290	50
DS04	0.8	0.40	35	1.2	2.12	250	55
DS05	1.0	0.50	40	1.2	2.55	290	50

The films were deposited on silicon substrates coated with silica (~ 70 nm), followed by heat treatment at temperatures of 900 °C to 1200 °C for 30 seconds in rapid thermal annealing system. The role of the silica interlayer in these films is twofold. First, it provides good optical confinement due to its lower refractive index than silicates (ranging between 1.68 and 1.75), as shown in the ellipsometry results given in Figure 4.1. Second, it enhances the luminescence efficiency by limiting interfacial reactions between the substrate and the film [86]

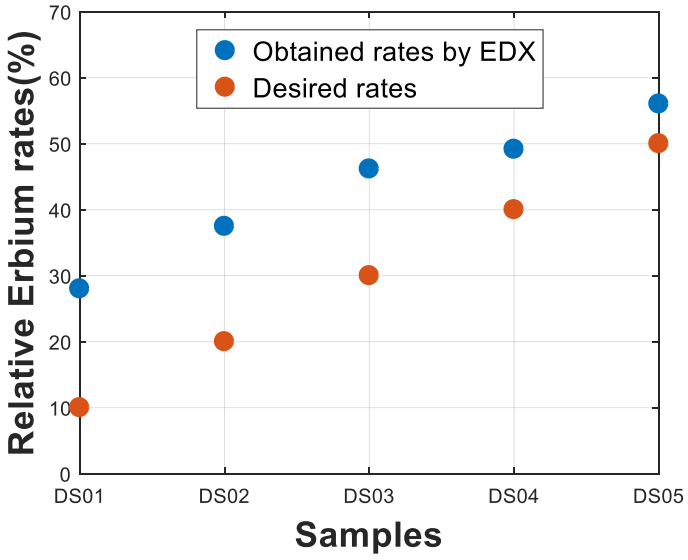

Figure 4.2. Obtained and targeted erbium-ytterbium ratios

4.3 Structural Properties

X-ray diffraction (XRD) and Raman analyses were performed to investigate the structural properties of erbium-ytterbium disilicates ($Er_xYb_{2-x}Si_2O_7$). The XRD was implemented for three samples (x= 0.92, 0.98, and 1.12 are labeled as DS03, DS04 and DS05, respectively) annealed twice at 1200^0C for 30 seconds. Although there was a difference between the obtained and desired erbium-ytterbium ratios, as discussed in the previous section, XRD results were well-matched with the monoclinic phase $Er_2Si_2O_7$ and $Yb_2Si_2O_7$ patterns, known as β- disilicate in the literature [109], [110]. Figure 4.3 demonstrates XRD patterns of the samples and β-disilicate phases in the Powder Diffraction File (PDF) database. The peaks of XRD shift to higher angles while the erbium concentration decrease because erbium atom is larger than ytterbium as seen from the differences in the position of DS03' peaks and other samples'. However, there is not any observable shift between the peaks of DS04 and DS05.

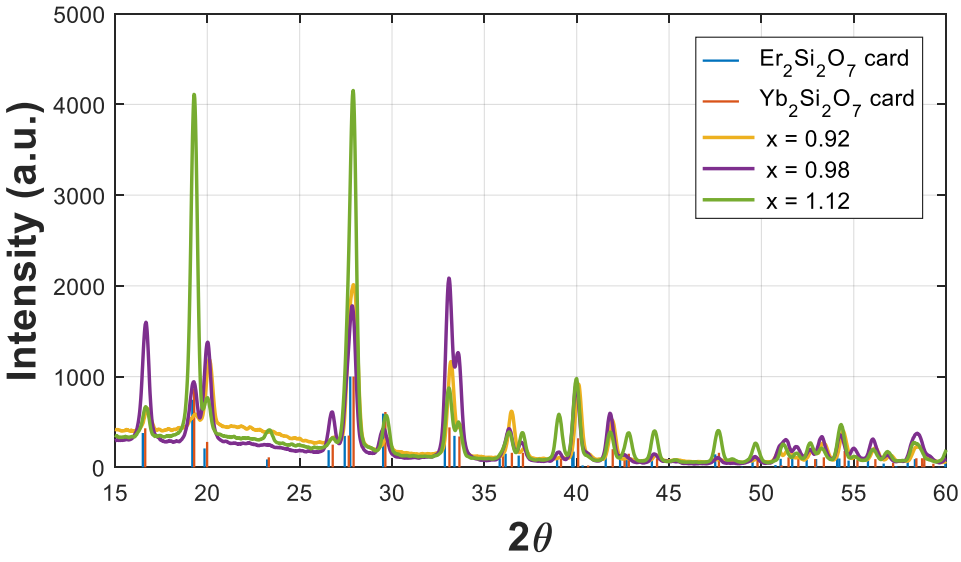

Figure 4.3. XRD patterns of three samples (x= 0.92, 0.98, and 1.12) annealed twice at 1200^0C for 30 seconds and β-disilicate phases in the Powder Diffraction File (PDF) database. The inset shows a zoom for low intensities.

Figure 4.4 shows the Raman spectra of the erbium-ytterbium disilicates ($Er_xYb_{2-x}Si_2O_7$) annealed twice at 1200 ^{0}C. The figure demonstrates that the Raman patterns for all of the $Er_xYb_{2-x}Si_2O_7$ films match each other and the spectrum of beta phase disilicate reported in the literature [110]. In other words, Raman measurements indicate that all films were crystallized in the β-disilicate phase. In addition to the phase of the films, the effect of annealing temperature on crystallinity was investigated by Raman measurements. The measurements indicate that the crystallization temperature for the films is 1200 ^{0}C, as shown in Figure 4.5. The figure shows Raman spectra of the samples annealed at temperatures of 900 ^{0}C to 1200 ^{0}C with a composition of x=0.92 (labeled as DS03).

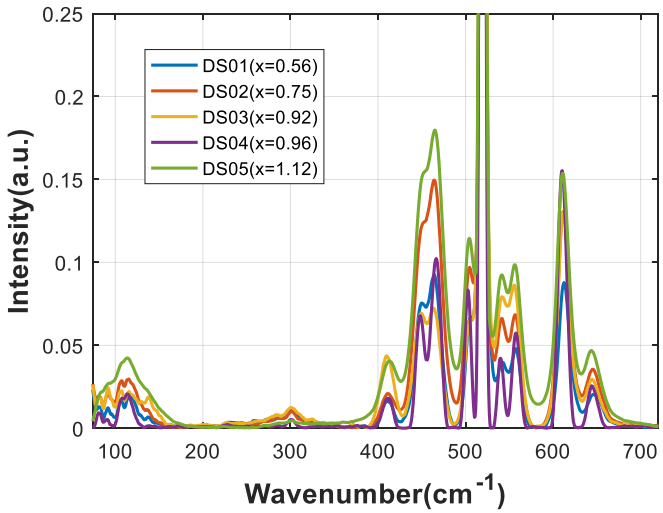

Figure 4.4. Raman spectra of the erbium-ytterbium disilicates annealed twice at 1200 ^{0}C

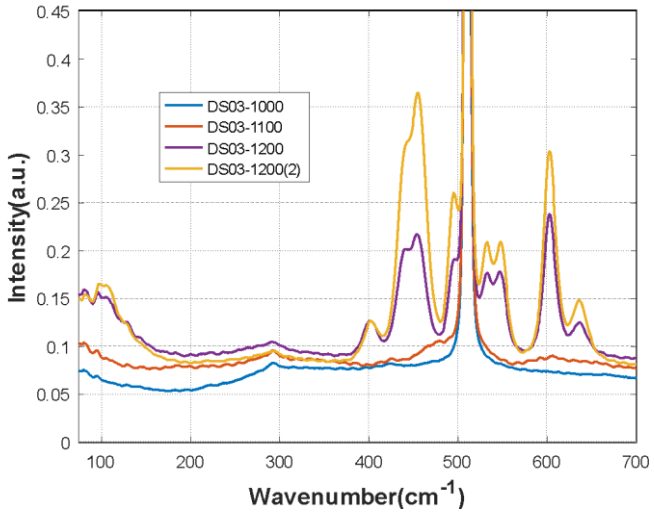

Figure 4.5. Raman spectra of $Er_{0.92}Yb_{1.18}Si_2O_7$ annealed at 1000, 1100, 1200 ^oC and annealed twice at 1200 ^oC

4.4 Photoluminescence Properties

4.4.1 PL Emission Properties

The PL emission spectra of erbium-ytterbium disilicates ($Er_xYb_{2-x}Si_2O_7$), annealed twice at 1200 ^0C, are given in Figure 4.6. As shown in the figure, the PL intensity increases monotonically with erbium concentration up to the optimum value of x=0.92. When the erbium concentration increases above this value, the PL intensity decreases. This can be explained by two mechanisms. First, increasing erbium concentration raises the PL intensity because erbium is the luminescence center in the crystal. However, the increasing concentration also enhances high energy transfer rates, hence increasing the effect of quenching centers. Secondly, decreasing ytterbium concentration reduces total absorption since the absorption cross-section of ytterbium is an order of higher magnitude than that of erbium at 980 nm.

The second noteworthy trend in the figure is the shapes of spectra. As mentioned in chapter 2, lanthanides' excited levels split into several sublevels because of the crystal-field, so the exact position of them is determined by the phase of the silicate.

In addition to XRD and Raman analyses, the similar shapes of PL spectra indicate that all films are in the β-disilicate phase.

Figure 4.7 depicts the PL emission spectrum of two disilicate films annealed at temperatures of 900 ^{0}C to 1200 ^{0}C with a concentration of x = 0.92 and 0.96. The figure clearly demonstrates that the PL intensity of the disilicates depends strongly on the annealing temperature, i.e., crystallinity. PL emissions from silicates annealed at temperatures below the crystallization temperature were not observed. Moreover, the spectra of films were annealed one and twice at 1200 ^{0}C varied in intensity, while the shapes of spectra remained the same.

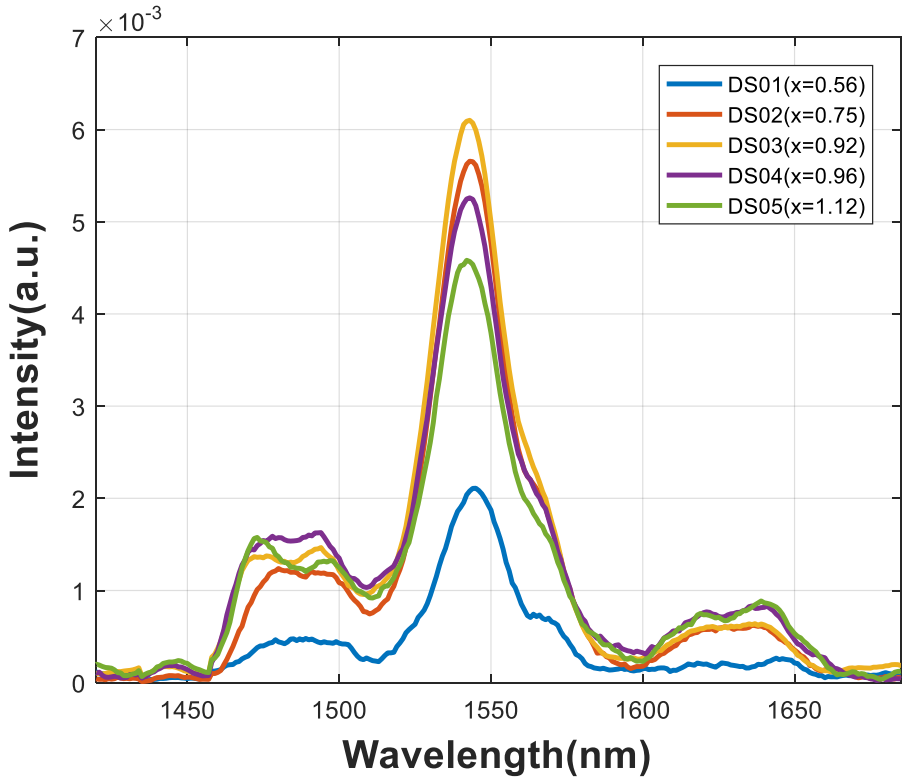

Figure 4.6. PL emission spectra of erbium-ytterbium disilicates ($Er_xYb_{2-x}Si_2O_7$) annealed twice at 1200 ^{0}C under 975 nm excitation.

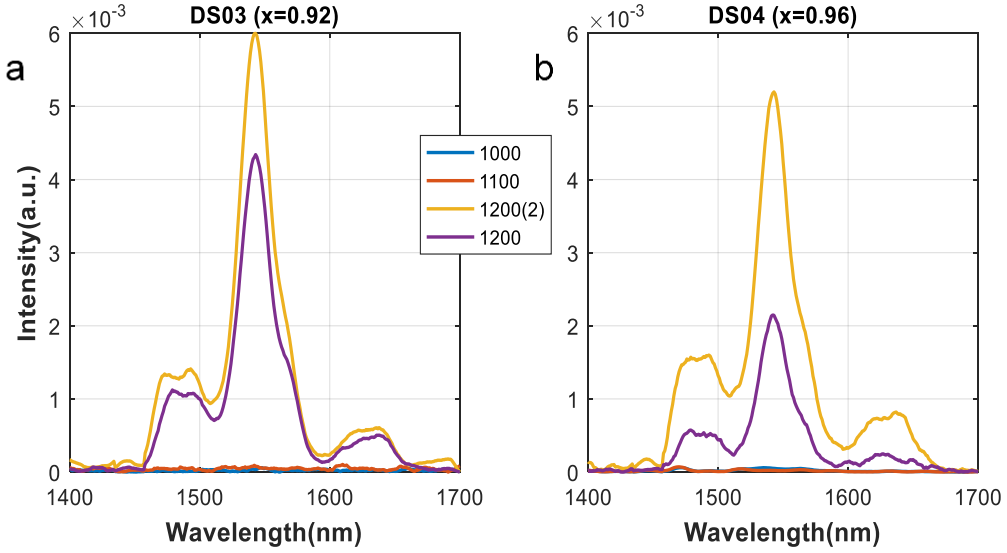

Figure 4.7. PL emission spectrum of two disilicate films annealed at temperatures of 900 ^{0}C to 1200 ^{0}C with a concentration of (a) x = 0.92 and (b) 0.96

4.4.2 PL Upconversion Properties

Figure 4.8 is the energy schemes of Er^{3+} and Yb^{3+}, explaining the upconversion mechanism under 1545 nm excitation assigned to the Er^{3+} $4I_{13/2} \rightarrow 4I_{15/2}$ transition. The sequential absorption of two photons by an Er^{3+} ion (i.e., ESA), and the energy transfer between two initially excited Er^{3+} ions (i.e., ETU), are the two main mechanisms of NIR-NIR upconversion in the system. Under the excitation of a 1545 nm laser, the $^4I_{9/2}$ state is populated by these mechanisms. Typically, the transitions are followed by rapid multiphonon nonradiative relaxations due to the high phonon energy of SiO_2 (1100 cm^{-1}) and very low energy variation between $^4I_{9/2}$ and $^4I_{11/2}$ states.

The role of ytterbium in NIR-NIR upconversion is threefold. Firstly, it is used for dilution of erbium ions to decrease concentration quenching effects and to increase the lifetime of the $^4I_{13/2}$ state. The high lifetime of the first excited state raises the probability of sequential absorption, increasing the upconversion rate. Secondly, ytterbium ions reduce the cross-relaxation probability of the $^4I_{11/2}$ state due to the

absence of an intermediate level. Thirdly, the high emission cross-section of ytterbium ion at 980 nm decreases the lifetime of the state and the upconversion probability above this level.

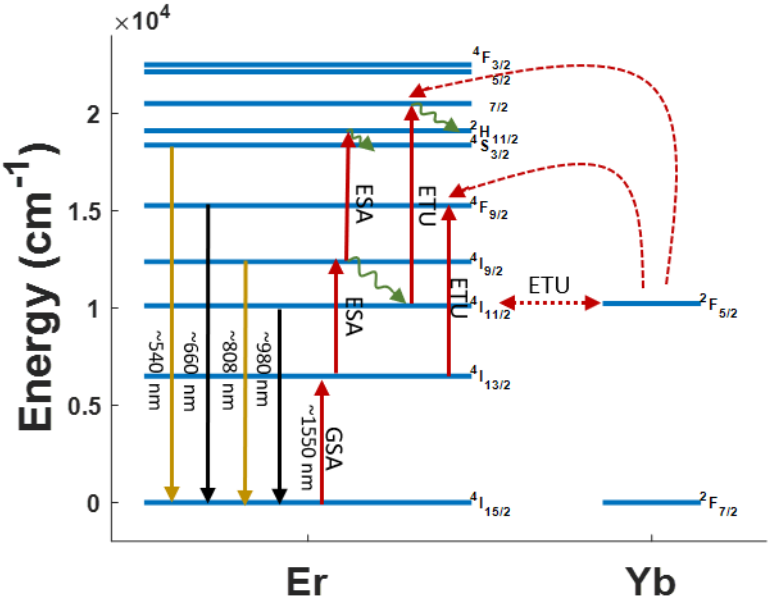

Figure 4.8. The energy schemes of Er^{3+} and Yb^{3+}, explaining the upconversion mechanism under ~1550 nm excitation. The solid red, dashed red, curved green, black and yellowish lines represent absorptions, energy transfers, multiphonon relaxations, and emissions, respectively.

As a result of the above-mentioned effects of ytterbium ion and multiphonon relaxations occurring between $^4I_{9/2}$ and $^4I_{11/2}$ states, upconversion emission only at 980 nm was observed, as shown in Figure 4.9. We investigated the upconversion luminescence at different concentrations and annealing temperatures. The same trend was observed for upconversion and emission PL intensities, in terms of both annealing temperature and ion concentration. Figure 4.9 demonstrates that the PL intensity increased with the concentration of erbium up to x=0.92 and then saturated and subsequently decreased depending on erbium concentration. Figure 4.10 shows the PL emission spectrum of four disilicate films annealed at temperatures of 900 ^{0}C to 1200 ^{0}C with concentration of x = 0.56, 0.75, 0.92 and 0.96. It is worth noting that

the upconversion intensities show similar changes to the emission, so upconversion emission was not observed below 1200 ^{0}C annealing temperatures.

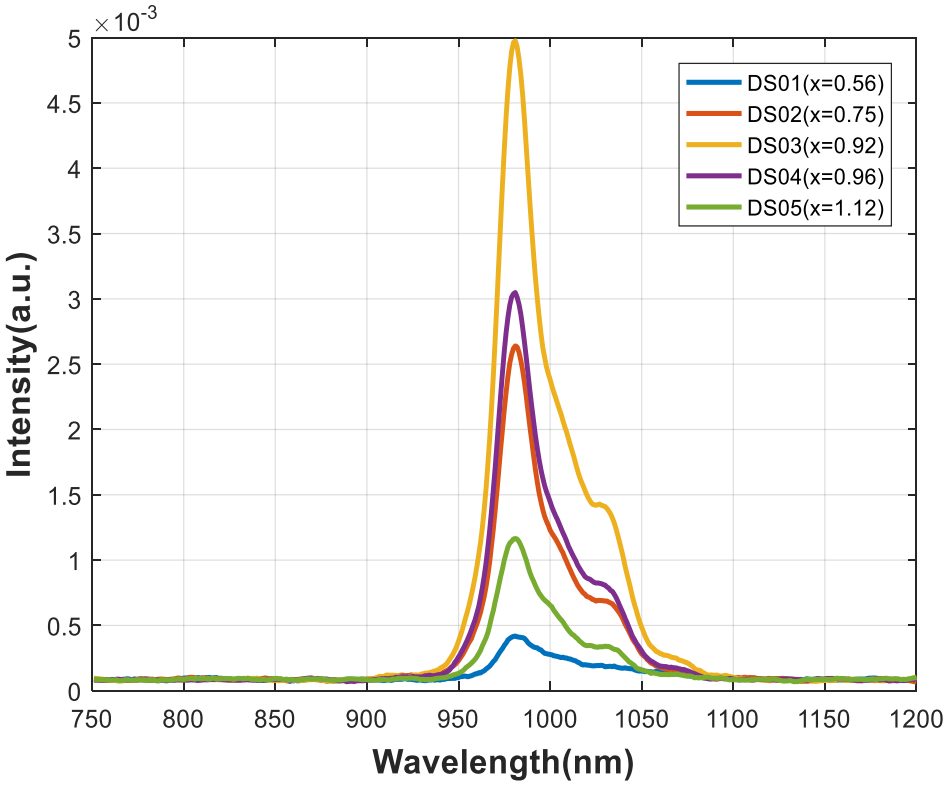

Figure 4.9. PL upconversion spectra of erbium-ytterbium disilicate thin films annealed twice at 1200 ^{0}C with varying compositions (x in $Er_xYb_{2-x}Si_2O_7$) under 975 nm excitation.

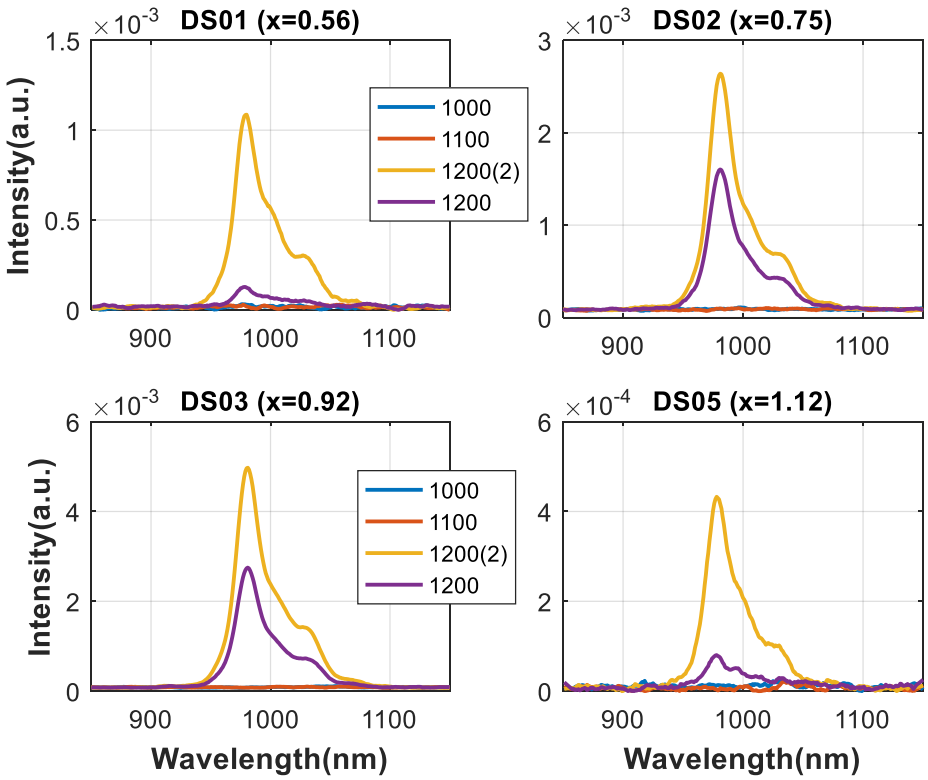

Figure 4.10. PL upconversion spectra of four disilicate films annealed at temperatures with concentration of x = 0.56, 0.75, 0.92 and 0.96.

4.4.3 PL Dependence on Excitation Power

The power-dependent PL measurements were performed on the sample with the highest upconversion intensity and x = 0.92. The integrated PL emission intensity over the main erbium emission lobe as a function of pump power of a 975 nm laser is given in Figure 4.11. It shows a linear dependence between excitation power and PL intensity. The linear relation between the PL intensity and the excitation power can be explained by investigating the rate equation for the first excited level of an upconverter sample (described in chapter 2), where the population change is given by the expression:

$$\frac{dN_1}{dt} = \sigma\Phi(N_{Er} - N_1) - \frac{N_1}{\tau_1} - C_{up}{N_1}^2 \qquad (4.1)$$

where N_1 is the population of the first level, σ is the absorption cross-section (in cm^2**),** Φ is the pump photon flux (in $cm^{-2}s^{-1}$), N_{Er} is the number of erbium ions, τ_1 is the lifetime of the first excited state (in s) and C_{up} is s the upconversion coefficient (in cm^3s^{-1}).

The solution of the quadratic equation in steady-state regime is given by:

$$N_1 = \frac{-(1 + \sigma\Phi\tau_1) + \sqrt{(1 + \sigma\Phi\tau_1)^2 + 4C_{up}\sigma\Phi{\tau_1}^2 N_{Er}}}{2C_{up}\tau_1} \qquad (4.2)$$

The square root can be simplified by Taylor expansion, and the exponential terms in the expression can be neglected at a low value of $\sigma\Phi$. We can rewrite the formula for the population of the first excited state as:

$$N_1 = \sigma\Phi\tau_1 N_{Er} \qquad (4.3)$$

Since the population of the first excited state is directly proportional to the PL intensity, we can write:

$$I \propto \sigma\Phi\tau_1 N_{Er} \qquad (4.4)$$

Finally, Equation 4.4 presents the linear relation, confirmed experimentally by obtaining power dependence between the PL intensity and the excitation power. Unlike our study results, Vanhoutte [109] has been demonstrated a sub-linear curve, and he associated it with upconversion. It is clear from Equation 4.1 that $N_{Er} - N_1$ and C_{up} are two factors that disturb the linearity. The first expression shows the number of available states, and as the value decreases, the intensity saturates. The second expression demonstrates the upconversion coefficient that depletes the first excited state and causes sub-linearity of the PL intensity. We believe that the mentioned difference with the literature can be explained by the first factor since he used an excitation wavelength of 488 nm, which does not allow sequential absorption due to the absence of energy levels at around 244 nm. Therefore, the available states were saturated, and the sub-linear curve was observed.

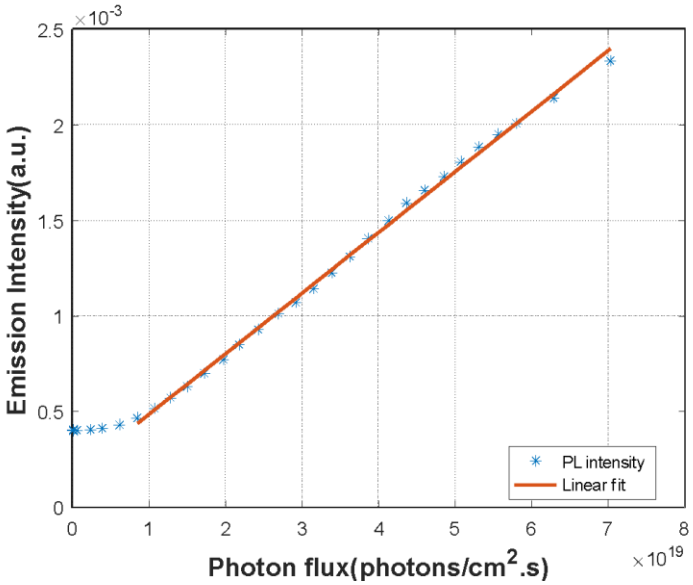

Figure 4.11. Integrated PL emission intensity of $Er_{0.92}Yb_{1.08}Si_2O_7$ as a function of pump power of the 975 nm laser. The fitted linear curve shows high level of linearity of the dependence.

In addition to PL emission intensity, the excitation power dependence of the PL upconversion intensity was performed. Figure 4.12 shows the integrated PL upconversion intensity around the peak at 980 nm as a function of the pump power of a 1545 nm laser. Equation 4.1 clearly indicates that the number of upconverted photons is quadratically related to the population of the first excited state. Therefore, the PL upconversion intensity demonstrates a quadratic dependence on the excitation power when transitions to upper levels are negligible, and radiative transitions are dominant compared to non-radiative losses. As mentioned in the previous section, we can neglect the transitions to upper states due to the high emission rate of ytterbium at the upconverted state ($^4I_{13/2}$). Generally, the relation between PL upconversion intensity and pump power is expressed as the following:

$$I_{UC} \propto P^n \tag{4.5}$$

where n is the number of photons required to excite the upconverted level. As shown in Figure 4.12, the experimentally obtained data fits well to a power function y =

ax^2-b. Here, a and b are constants, and b represents background noise. The best fit confirms that there is a two-photon upconversion process.

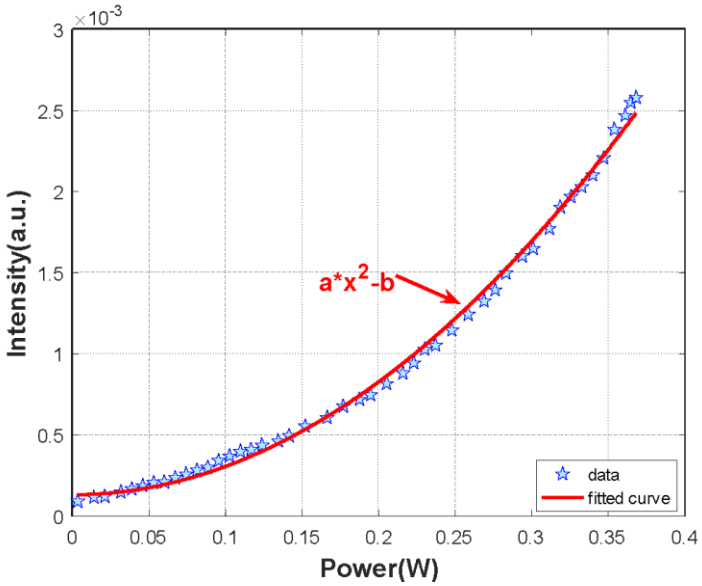

Figure 4.12. Integrated PL upconversion intensity of $Er_{0.92}Yb_{1.08}Si_2O_7$ as a function of pump power. The red line represents the best fit of the experimental data. The quadratic dependence indicates a purely two-photon process.

4.4.4 PL Lifetime Results

Although time-domain methods are widely used in the literature, we took the lifetime measurements in the frequency domain due to some constraints. The first limitation was that the voltage of the photodiode (as low as 5 microvolts) was lower than the noise. Therefore, we employed an SR830 lock-in amplifier from Stanford Research Systems, Inc. (Sunnyvale, CA, United States) with tolerable noise up to 100 dB and a minimum detectable Voltage of 2nV. The second limitation was that we did not have a light source that can be modulated by the Sine wave. Eventually, we used the method described in detail in chapter 3. However, to use the method, the rising and decaying lifetimes must be equal. As mentioned earlier, rising and decaying lifetimes are equal at low upconversion emissions and low pump powers. Figure 4.13 shows the variation of the Y-out with different pump powers. The overlapping of results at

different pump powers allows high-power measurements that increase the signal according to noise ratio. The signal-to-noise ratio enhancement with increasing pump power is given in Figure 4.14.

Therefore, we first made all measurements at high pump power. Later, the lifetime of the sample with the highest upconversion was measured at low power. The consequence of upconversion is decrease in lifetime with the increase of the pump power, as seen in Equation 4.1. The difference caused by this decrease was added to the measured lifetimes of other samples at high power. Table 4 shows the lifetime of the samples at the first excited state ($^4I_{13/2}$ corresponds to a wavelength of around 1540 nm). The lifetimes of the samples followed a trend where the increased concentration of ytterbium reduced the rate of energy transfer in the first excited state, thereby reducing non-radiative decay paths. Therefore, the lifetimes increased with the ytterbium rate.

Table 4.2 The lifetime of the samples at the first excited state (in ms)

DS01 (x = 0.56)	DS02 (x = 0.75)	DS03 (x=0.92)	DS04 (x=0.96)	DS05 (x=1.12)
3.1+0.025	2.93+0.025	2.75+0.025	2.65+0.025	2.50+0.025

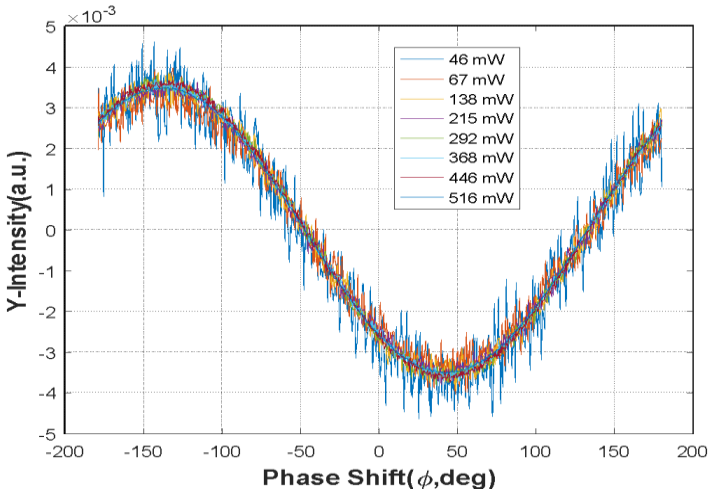

Figure 4.13. The variation of the Y-out as a function of phase shift with different pump powers

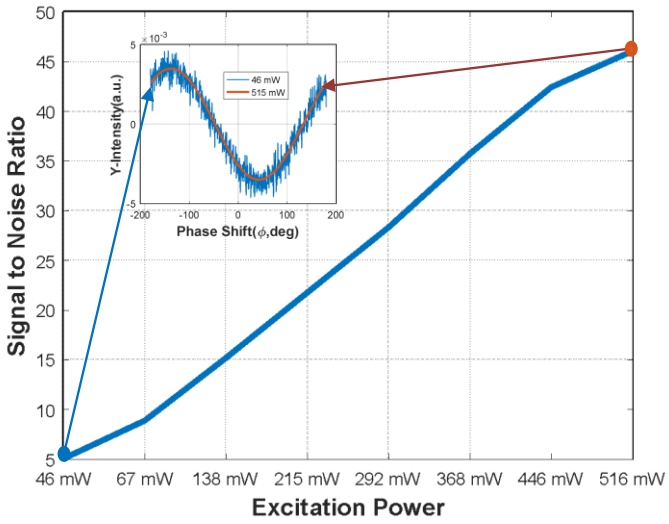

Figure 4.14. Excitation power dependence of Signal to Noise Ratio

CHAPTER 5

SUMMARY AND CONCLUSIONS

Upconversion materials absorb lower energy photons and convert them to a fewer number of higher energy photons, which can have interesting applications in solar cells, biological imaging, 3D display, and infrared sensing. Materials consisting of crystals doped with lanthanide ions are generally used as upconversion material since multiple energy levels of lanthanide ions allow sequential absorption, and the long lifetimes of these levels increase the probability of energy transfer upconversion.

In this thesis, erbium-ytterbium disilicate ($Er_xYb_{2-x}Si_2O_7$) compounds were investigated as material systems for the development of chemically, mechanically and thermally stable upconverter materials. Up until now, the upconversion properties of erbium-ytterbium silicates have not been extensively investigated since they are considered as a candidate for waveguide material rather than an upconversion material. Although the upconversion efficiency of the silicates suffers from the high phonon energy of silica, we have used them due to the stability and non-toxic nature of oxides. After selecting the host material, we chose erbium and ytterbium as doping ions. Erbium is used as an activator because its ladder-like arrangement of energy levels with close energy gaps enhances upconversion efficiency. Ytterbium is used as a diluting ion due to its threefold role. Firstly, dilution of erbium ions increases the lifetime of their first excited state, thereby increasing the efficiency of the upconversion. Secondly, ytterbium ions reduce cross-relaxation probability due to the absence of an intermediate level. Thirdly, the high emission cross-section of ytterbium ion at 980 nm decreases the lifetime of the state and the upconversion probability above that level.

Erbium-Ytterbium silicate thin films were deposited using reactive rf-magnetron co-sputtering of Er_2O_3, SiO_2, and Yb targets and analyzed structurally and optically.

EDX, XRD, and Raman were performed to investigate the structural properties of these films. EDX results showed that the films with desired stoichiometries and thickness could not be produced, while XRD and Raman results indicated that the films crystallized into the monoclinic phase $Er_2Si_2O_7$ and $Yb_2Si_2O_7$, known as β-$Er_2Si_2O_7$ in the literature. Furthermore, it was observed from Raman measurements that the crystallization temperature of disilicates lies between 1100 and 1200 ^{0}C.

PL measurements were recorded under 975 nm and 1545 nm lasers to obtain PL emission and upconversion patterns, respectively. A rapid increase in both PL intensities was observed with annealing temperature, attributed to enhanced crystallinity. Moreover, we analyzed the influence of different doping concentrations on the PL upconversion and emission intensities. We observed pure NIR-NIR upconversion from all samples, including $Er_{0.75}Yb_{1.25}Si_2O_7$ with a thickness of 110 nm. To the best of our knowledge, the only other study - exists in the literature showing an upconversion for the thin film erbium-ytterbium silicates - utilized films at 450 nm (Vanhoutte et al. [87]). Therefore, we can conclude that this is the first demonstration of upconversion for the thin film erbium-ytterbium silicates as thin as 110 nm. All films made in this work show pure NIR-NIR upconversion, which is considered to be more efficient in various applications in the literature, including bioimaging and fingerprint detection.

In addition to PL spectra, PL lifetimes of samples were measured with an advanced method. This method combines square wave excitation and a lock-in amplifier to measure lifetime, which allows real-time lifetime measurements. It was observed that the lifetime decreases with the increase of the erbium rate. This reduction has been attributed to the increase of non-radiative decay paths as a result of the raised energy transfer rate.

Finally, we conclude that the upconversion efficiencies of erbium-ytterbium silicates are low. While they may not seem suitable for well-known upconversion applications, they could be the sought-after material for new applications that need

more precision due to their pure upconversion property. For instance, they can be used by coupling with a cheap silicon detector to detect photons beyond 1.1 μm.

5.1 Outlook

Despite the enormous efforts spent on upconversion materials, there are still many challenges to realizing current upconversion applications. The major challenge is the low absorption cross-section of lanthanides resulting in low quantum efficiency. Future research should focus on enhancing the efficiency either by adding sensitizers with high absorption cross-sections or by using host matrices that efficiently absorb incident photons and transfer them to lanthanides. Adding sensitizers is already a common method, but it limits the number of activators (Erbium in our case) in the matrix. Therefore, the use of a direct bandgap material, where the bandgap is resonant to the interested level of the activator, as a host matrix should be investigated.

REFERENCES

[1] N. Bloembergen, “Solid State Infrared Quantum Counters,” *Phys. Rev. Lett.*, vol. 2, no. 3, pp. 84–85, Feb. 1959.

[2] W. G. van Sark, J. de Wild, J. K. Rath, A. Meijerink, and R. E. Schropp, “Upconversion in solar cells,” *Nanoscale Res. Lett.*, 2013.

[3] M. González-Béjar, L. Francés-Soriano, and J. Pérez-Prieto, “Upconversion nanoparticles for bioimaging and regenerative medicine,” *Frontiers in Bioengineering and Biotechnology*. 2016.

[4] M. Sharipov, S. M. Tawfik, Z. Gerelkhuu, B. T. Huy, and Y. I. Lee, “Phospholipase A2-Responsive Phosphate Micelle-Loaded UCNPs for Bioimaging of Prostate Cancer Cells,” *Sci. Rep.*, 2017.

[5] J. Y. Allain, M. Monerie, and H. Poignant, “Blue Upconversion Fluorozirconate Fibre Laser,” *Electron. Lett.*, 1990.

[6] S. Balabhadra, M. L. Debasu, C. D. S. Brites, R. A. S. Ferreira, and L. D. Carlos, “Upconverting Nanoparticles Working As Primary Thermometers in Different Media,” *J. Phys. Chem. C*, 2017.

[7] Y. Yang, Y. H. Zhang, W. Z. Shen, and H. C. Liu, “Semiconductor infrared up-conversion devices,” *Progress in Quantum Electronics*. 2011.

[8] L. Høgstedt, A. Fix, M. Wirth, C. Pedersen, and P. Tidemand-Lichtenberg, “Upconversion-based lidar measurements of atmospheric CO_2,” *Opt. Express*, 2016.

[9] R. Deng, F. Qin, R. Chen, W. Huang, M. Hong, and X. Liu, “Temporal full-colour tuning through non-steady-state upconversion,” *Nat. Nanotechnol.*, 2015.

[10] M. Wolf, “A new look at silicon solar cell performance,” *Energy Convers.*, vol. 11, no. 2, pp. 63–73, Jun. 1971.

[11] T. Takamoto, E. Ikeda, H. Kurita, and M. Ohmori, “Over 30% efficient InGaP/GaAs tandem solar cells,” *Appl. Phys. Lett.*, vol. 70, no. 3, pp. 381–383, 1997.

[12] L. Wang *et al.*, “Current and efficiency improvement for a GaAsP/SiGe on Si tandem solar cell device achieved by light trapping techniques,” *Phys. status solidi – Rapid Res. Lett.*, vol. 10, no. 8, pp. 596–599, 2016.

[13] S. Albrecht *et al.*, “Efficient hybrid inorganic/organic tandem solar cells with tailored recombination contacts,” *Sol. Energy Mater. Sol. Cells*, vol. 127, pp. 157–162, Aug. 2014.

[14] V. I. Klimov, “Mechanisms for Photogeneration and Recombination of Multiexcitons in Semiconductor Nanocrystals: Implications for Lasing and Solar Energy Conversion,” *J. Phys. Chem. B*, vol. 110, no. 34, pp. 16827–16845, Aug. 2006.

[15] A. Luque and A. Martí, “Increasing the Efficiency of Ideal Solar Cells by Photon Induced Transitions at Intermediate Levels,” *Phys. Rev. Lett.*, 1997.

[16] B. M. Van Der Ende, L. Aarts, and A. Meijerink, “Lanthanide ions as spectral converters for solar cells,” *Phys. Chem. Chem. Phys.*, 2009.

[17] Y. Shang, S. Hao, C. Yang, and G. Chen, “Enhancing solar cell efficiency using photon upconversion materials,” *Nanomaterials*. 2015.

[18] H. S. Jung, G. S. Han, N.-G. Park, and M. J. Ko, “Flexible Perovskite Solar Cells,” *Joule*, vol. 3, no. 8, pp. 1850–1880, Aug. 2019.

[19] B. van der Zwaan and A. Rabl, “Prospects for PV: a learning curve analysis,” *Sol. Energy*, vol. 74, no. 1, pp. 19–31, Jan. 2003.

[20] A. Goetzberger, C. Hebling, and H.-W. Schock, “Photovoltaic materials, history, status and outlook,” *Mater. Sci. Eng. R Reports*, vol. 40, no. 1, pp. 1–46, Jan. 2003.

[21] W. Shockley and H. J. Queisser, “Detailed balance limit of efficiency of p-n junction solar cells,” *J. Appl. Phys.*, 1961.

[22] M. A. Green *et al.*, “Solar cell efficiency tables (Version 53),” *Prog. Photovoltaics Res. Appl.*, vol. 27, no. 1, pp. 3–12, 2019.

[23] K. Yoshikawa *et al.*, “Silicon heterojunction solar cell with interdigitated back contacts for a photoconversion efficiency over 26%,” *Nat. Energy*, 2017.

[24] G. Chen, J. Seo, C. Yang, and P. N. Prasad, “Nanochemistry and nanomaterials for photovoltaics,” *Chemical Society Reviews*. 2013.

[25] T. Trupke, M. A. Green, and P. Würfel, “Improving solar cell efficiencies by down-conversion of high-energy photons,” *J. Appl. Phys.*, 2002.

[26] T. Trupke, M. A. Green, and P. Würfel, “Improving solar cell efficiencies by up-conversion of sub-band-gap light,” *J. Appl. Phys.*, 2002.

[27] T. F. Schulze and T. W. Schmidt, “Photochemical upconversion: Present status and prospects for its application to solar energy conversion,” *Energy and Environmental Science*. 2015.

[28] J. C. Goldschmidt and S. Fischer, “Upconversion for photovoltaics - a review of materials, devices and concepts for performance enhancement,” *Advanced Optical Materials*. 2015.

[29] J. C. Goldschmidt *et al.*, “Experimental analysis of upconversion with both coherent monochromatic irradiation and broad spectrum illumination,” *Sol.*

Energy Mater. Sol. Cells, vol. 95, no. 7, pp. 1960–1963, Jul. 2011.

[30] D. Wang, J. F. Chen, and L. Dai, "Recent advances in graphene quantum dots for fluorescence bioimaging from cells through tissues to animals," *Part. Part. Syst. Charact.*, 2015.

[31] M. V. DaCosta, S. Doughan, Y. Han, and U. J. Krull, "Lanthanide upconversion nanoparticles and applications in bioassays and bioimaging: A review," *Analytica Chimica Acta*. 2014.

[32] F. Wang and X. Liu, "Recent advances in the chemistry of lanthanide-doped upconversion nanocrystals," *Chemical Society Reviews*. 2009.

[33] E. Thimsen, B. Sadtler, and M. Y. Berezin, "Shortwave-infrared (SWIR) emitters for biological imaging: A review of challenges and opportunities," *Nanophotonics*. 2017.

[34] A. Gnach, T. Lipinski, A. Bednarkiewicz, J. Rybka, and J. A. Capobianco, "Upconverting nanoparticles: assessing the toxicity," *Chem. Soc. Rev.*, vol. 44, no. 6, pp. 1561–1584, 2015.

[35] F. Wang, D. Banerjee, Y. Liu, X. Chen, and X. Liu, "Upconversion nanoparticles in biological labeling, imaging, and therapy," *Analyst*. 2010.

[36] Y. Il Park *et al.*, "Nonblinking and nonbleaching upconverting nanoparticles as an optical imaging nanoprobe and T1 magnetic resonance imaging contrast agent," *Adv. Mater.*, 2009.

[37] S. Hohng and T. Ha, "Near-Complete Suppression of Quantum Dot Blinking in Ambient Conditions," *J. Am. Chem. Soc.*, 2004.

[38] Y. Ning, M. Zhu, and J. L. Zhang, "Near-infrared (NIR) lanthanide molecular probes for bioimaging and biosensing," *Coordination Chemistry Reviews*. 2019.

[39] C. Cao, Q. Liu, M. Shi, W. Feng, and F. Li, "Lanthanide-Doped Nanoparticles with Upconversion and Downshifting Near-Infrared Luminescence for Bioimaging," *Inorg. Chem.*, vol. 58, no. 14, pp. 9351–9357, Jul. 2019.

[40] Q. Hu, J. Seidelin Dam, C. Pedersen, and P. Tidemand-Lichtenberg, "High-resolution mid-IR spectrometer based on frequency upconversion," *Opt. Lett.*, 2012.

[41] J. S. Dam, P. Tidemand-Lichtenberg, and C. Pedersen, "Room-temperature mid-infrared single-photon spectral imaging," *Nat. Photonics*, 2012.

[42] M. Wu, "Infrared-to-Visible Upconversion in Hybrid Thin Films of Colloidal Nanocrystals and Organic Molecules," Massachusetts Institute of Techonology, 2018.

[43] S. A. Wade, S. F. Collins, and G. W. Baxter, "Fluorescence intensity ratio

technique for optical fiber point temperature sensing," *Journal of Applied Physics*. 2003.

[44] W. Xu, H. Zhao, Z. Zhang, and W. Cao, "Highly sensitive optical thermometry through thermally enhanced near infrared emissions from Nd3+/Yb3+ codoped oxyfluoride glass ceramic," *Sensors Actuators B Chem.*, vol. 178, pp. 520–524, Mar. 2013.

[45] V. K. Rai, "Temperature sensors and optical sensors," *Appl. Phys. B*, vol. 88, no. 2, pp. 297–303, Jul. 2007.

[46] Y. Zhao, X. Wang, Y. Zhang, Y. Li, and X. Yao, "Optical temperature sensing of up-conversion luminescent materials: Fundamentals and progress," *Journal of Alloys and Compounds*. 2020.

[47] F. Sidiroglou, S. A. Wade, N. M. Dragomir, G. W. Baxter, and S. F. Collins, "Effects of high-temperature heat treatment on Nd3+-doped optical fibers for use in fluorescence intensity ratio based temperature sensing," *Rev. Sci. Instrum.*, vol. 74, no. 7, pp. 3524–3530, 2003.

[48] M. Runowski, A. Bartkowiak, M. Majewska, I. R. Martín, and S. Lis, "Upconverting lanthanide doped fluoride NaLuF4:Yb3+-Er3+-Ho3+ - optical sensor for multi-range fluorescence intensity ratio (FIR) thermometry in visible and NIR regions," *J. Lumin.*, vol. 201, pp. 104–109, Sep. 2018.

[49] L. Marciniak, A. Bednarkiewicz, and W. Strek, "Tuning of the up-conversion emission and sensitivity of luminescent thermometer in LiLaP4O12:Tm,Yb nanocrystals via Eu3+ dopants," *J. Lumin.*, 2017.

[50] S. A. Wade, J. C. Muscat, S. F. Collins, and G. W. Baxter, "Nd3+-doped optical fiber temperature sensor using the fluorescence intensity ratio technique," *Rev. Sci. Instrum.*, 1999.

[51] G. S. Maciel *et al.*, "Temperature Sensor Based on Frequency Upconversion in Er3+-Doped Fluoroindate Glass," *IEEE Photonics Technol. Lett.*, 1995.

[52] D. Manzani, J. F. da S. Petruci, K. Nigoghossian, A. A. Cardoso, and S. J. L. Ribeiro, "A portable luminescent thermometer based on green up-conversion emission of Er3+/Yb3+ co-doped tellurite glass," *Sci. Rep.*, vol. 7, no. 1, p. 41596, 2017.

[53] E. Downing, L. Hesselink, J. Ralston, and R. Macfarlane, "A three-color, solid-state, three-dimensional display," *Science (80-.).*, 1996.

[54] X. Chen *et al.*, "Initital research of three-dimensional volumetric display based on di-frequency upconversion," in *Display Devices and Systems II*, 1998, vol. 3560, pp. 122–131.

[55] G. S. Maciel, A. Biswas, R. Kapoor, and P. N. Prasad, "Blue cooperative upconversion in Yb3+-doped multicomponent sol-gel-processed silica glass

for three-dimensional display," *Appl. Phys. Lett.*, vol. 76, no. 15, pp. 1978–1980, 2000.

[56] X. Liu, G. Dong, Y. Qiao, and J. Qiu, "Transparent colloid containing upconverting nanocrystals: An alternative medium for three-dimensional volumetric display," in *Applied Optics*, 2008.

[57] A. Edgar, "Luminescence materials," in *Springer Handbook of Electronic and Photonic Materials*, 2nd ed., S. Kasap and P. Capper, Eds. springer, 2017, pp. 997–1012.

[58] A. J. Kenyon, "Erbium in silicon," *Semiconductor Science and Technology*. 2005.

[59] S. Han, R. Deng, X. Xie, and X. Liu, "Enhancing luminescence in lanthanide-doped upconversion nanoparticles," *Angewandte Chemie - International Edition*. 2014.

[60] J. Bao, N. Yu, F. Capasso, T. Mates, M. Troccoli, and A. Belyanin, "Controlled modification of erbium lifetime in silicon dioxide with metallic overlayers," *Appl. Phys. Lett.*, 2007.

[61] I. Etchart, "Metal Oxides for Efficient Infrared to Visible Upconversion," University of Cambridge, 2010.

[62] G. H. Dieke and R. A. Satten, "Spectra and Energy Levels of Rare Earth Ions in Crystals," *Am. J. Phys.*, 1970.

[63] P. S. Peijzel, A. Meijerink, R. T. Wegh, M. F. Reid, and G. W. Burdick, "A complete 4fn energy level diagram for all trivalent lanthanide ions," in *Journal of Solid State Chemistry*, 2005.

[64] C. M. Dodson and R. Zia, "Magnetic dipole and electric quadrupole transitions in the trivalent lanthanide series: Calculated emission rates and oscillator strengths," *Phys. Rev. B - Condens. Matter Mater. Phys.*, 2012.

[65] G. Chen, H. Qiu, P. N. Prasad, and X. Chen, "Upconversion nanoparticles: Design, nanochemistry, and applications in Theranostics," *Chemical Reviews*. 2014.

[66] M. Haase and H. Schäfer, "Upconverting nanoparticles," *Angewandte Chemie - International Edition*. 2011.

[67] J. F. Suyver *et al.*, "Novel materials doped with trivalent lanthanides and transition metal ions showing near-infrared to visible photon upconversion," *Opt. Mater. (Amst).*, 2005.

[68] W. Zheng, B. Sun, Y. Li, R. Wang, and Y. Xu, "Multicolor tunable luminescence and laser-sensitization induced upconversion enhancement in Ln-doped Gd2O3 crystals for anti-counterfeiting," *Mater. Chem. Front.*, 2019.

[69] S. Tabanli and G. Eryurek, “Upconversion luminescence properties of Y2O3: Yb3+/Er3+/Tm3+ nanocrystal doped PMMA nanocomposites,” *J. Non. Cryst. Solids*, 2019.

[70] S. Heer, K. Kömpe, H. U. Güdel, and M. Haase, “Highly efficient multicolour upconversion emission in transparent colloids of lanthanide-doped NaYF4 nanocrystals,” *Adv. Mater.*, 2004.

[71] C. Li, Z. Quan, J. Yang, P. Yang, and J. Lin, “Highly Uniform and Monodisperse β-NaYF4:Ln3+ (Ln = Eu, Tb, Yb/Er, and Yb/Tm) Hexagonal Microprism Crystals: Hydrothermal Synthesis and Luminescent Properties,” *Inorg. Chem.*, vol. 46, no. 16, pp. 6329–6337, Aug. 2007.

[72] K. Lemański, M. Babij, and P. J. Dereń, “Upconversion emission of the GaN nanocrystals doped with rare earth ions,” *Solid State Sci.*, vol. 94, pp. 127–132, Aug. 2019.

[73] M. Miritello, P. Cardile, R. Lo Savio, and F. Priolo, “Energy transfer and enhanced 154 μm emission in Erbium-Ytterbium disilicate thin films,” *Opt. Express*, 2011.

[74] M. Miritello, R. Lo Savio, P. Cardile, and F. Priolo, “Enhanced down conversion of photons emitted by photoexcited Er xY2-xSi2O7 films grown on silicon,” *Phys. Rev. B - Condens. Matter Mater. Phys.*, 2010.

[75] T. Li, C.-F. Guo, Y.-M. Yang, L. Li, and N. Zhang, “Efficient green up-conversion emission in Yb3+/Ho3+ co-doped CaIn2O4,” *Acta Mater.*, vol. 61, no. 19, pp. 7481–7487, Nov. 2013.

[76] R. Calderón-Villajos, C. Zaldo, and C. Cascales, “Enhanced upconversion multicolor and white light luminescence in SiO 2-coated lanthanide-doped GdVO4 hydrothermal nanocrystals,” *Nanotechnology*, 2012.

[77] I. Etchart *et al.*, “Oxide phosphors for efficient light upconversion: Yb3+ and Er3+ co-doped Ln2BaZnO5 (Ln = Y, Gd),” *J. Mater. Chem.*, 2010.

[78] L. A. Riseberg and H. W. Moos, “Multiphonon orbit-lattice relaxation of excited states of rare-earth ions in crystals,” *Phys. Rev.*, 1968.

[79] A. Polman, “Erbium implanted thin film photonic materials,” *J. Appl. Phys.*, 1997.

[80] E. Snoeks, P. G. Kik, and A. Polman, “Concentration quenching in erbium implanted alkali silicate glasses,” *Opt. Mater. (Amst).*, 1996.

[81] F. Auzel, “Upconversion processes in coupled ion systems,” *J. Lumin.*, 1990.

[82] C. Strohhöfer and A. Polman, “Absorption and emission spectroscopy in Er3+ - Yb3+ doped aluminum oxide waveguides,” *Opt. Mater. (Amst).*, 2003.

[83] X. J. Wang *et al.*, “Extraordinary infrared photoluminescence efficiency of

Er0.1 Yb1.9 SiO5 films on SiO2/Si substrates," *Appl. Phys. Lett.*, 2011.

[84] H. Isshiki, M. J. A. De Dood, A. Polman, and T. Kimura, "Self-assembled infrared-luminescent Er-Si-O crystallites on silicon," in *Applied Physics Letters*, 2004.

[85] R. Lo Savio, M. Miritello, A. M. Piro, F. Priolo, and F. Iacona, "The influence of stoichiometry on the structural stability and on the optical emission of erbium silicate thin films," *Appl. Phys. Lett.*, 2008.

[86] M. Miritello *et al.*, "Efficient luminescence and energy transfer in erbium silicate thin films," *Adv. Mater.*, 2007.

[87] M. Vanhoutte, B. Wang, J. Michel, and L. C. Kimerling, "Processing and properties of ytterbium-erbium silicate thin film gain media," in *IEEE International Conference on Group IV Photonics GFP*, 2009.

[88] X. Wang, P. Zhou, Y. He, and Z. Zhou, "Erbium silicate compound optical waveguide amplifier and laser [Invited]," *Opt. Mater. Express*, 2018.

[89] K. Suh *et al.*, "Cooperative upconversion and optical gain in ion-beam sputter-deposited Er_xY_2-xSiO_5 waveguides," *Opt. Express*, 2010.

[90] X. J. Wang, G. Yuan, H. Isshiki, T. Kimura, and Z. Zhou, "Photoluminescence enhancement and high gain amplification of Er xY2-xSiO5 waveguide," *J. Appl. Phys.*, 2010.

[91] R. Guo, B. Wang, X. Wang, L. Wang, L. Jiang, and Z. Zhou, "Optical amplification in Er/Yb silicate slot waveguide," *Opt. Lett.*, vol. 37, no. 9, pp. 1427–1429, May 2012.

[92] B. Wang, G. Yuan, L. Wang, R. Guo, X. Wang, and Z. Zhou, "The Investigation on the 1.53 μm Photoluminescence of Magnetron-Sputtered Er0.2Re1.8Si2O7 (Re=Yb, Y) Thin Films," in *2011 Symposium on Photonics and Optoelectronics, SOPO 2011*, 2011.

[93] H. Sun *et al.*, "Giant optical gain in a single-crystal erbium chloride silicate nanowire," *Nat. Photonics*, 2017.

[94] P. D. Davidse and L. I. Maissel, "Dielectric thin films through RF sputtering," *J. Appl. Phys.*, 1966.

[95] J. George, *Preparation of Thin Films*. 1992.

[96] K. Strijckmans, R. Schelfhout, and D. Depla, "Tutorial: Hysteresis during the reactive magnetron sputtering process," *J. Appl. Phys.*, 2018.

[97] S. Berg and T. Nyberg, "Fundamental understanding and modeling of reactive sputtering processes," *Thin Solid Films*. 2005.

[98] A. Salimian, R. Haghpanahan, A. Hasnath, and H. Upadhyaya, "Optical analysis of RF sputtering plasma through colour characterization," *Coatings*,

2019.

[99] J. R. Lakowicz, *Principles of fluorescence spectroscopy*. 2006.

[100] M. J. Booth and T. Wilson, “Low-cost, frequency-domain, fluorescence lifetime confocal microscopy,” *J. Microsc.*, 2004.

[101] J. DiBenedetto, G. A. Capelle, and M. O’Neill, “Time-resolved hyperspectral fluorescence spectroscopy using frequency-modulated excitation,” *J. Appl. Phys.*, vol. 112, no. 1, p. 13109, 2012.

[102] C. M. McGraw, G. Khalil, and J. B. Callis, “Comparison of time and frequency domain methods for luminescence lifetime measurements,” *J. Phys. Chem. C*, 2008.

[103] N. Boens *et al.*, “Fluorescence lifetime standards for time and frequency domain fluorescence spectroscopy,” *Anal. Chem.*, 2007.

[104] J. Philip and K. Carlsson, “Theoretical investigation of the signal-to-noise ratio in fluorescence lifetime imaging,” *J. Opt. Soc. Am. A*, 2003.

[105] H. M. Rowe, S. P. Chan, J. N. Demas, and B. A. DeGraff, “Elimination of fluorescence and scattering backgrounds in luminescence lifetime measurements using gated-phase fluorometry,” *Anal. Chem.*, 2002.

[106] P. Jenkins, M. A. Naivar, and J. P. Houston, “Toward the measurement of multiple fluorescence lifetimes in flow cytometry: Maximizing multi-harmonic content from cells and microspheres,” *J. Biophotonics*, 2015.

[107] P. Harms, J. Sipior, N. Ram, G. M. Carter, and G. Rao, “Low cost phase-modulation measurements of nanosecond fluorescence lifetimes using a lock-in amplifier,” *Rev. Sci. Instrum.*, 1999.

[108] A. Esposito, H. C. Gerritsen, and F. S. Wouters, “Optimizing frequency-domain fluorescence lifetime sensing for high-throughput applications: photon economy and acquisition speed,” *J. Opt. Soc. Am. A*, 2007.

[109] M. Vanhoutte, “Erbium-ytterbium-yttrium compounds for light emission at 1.54pm,” Massachusetts Institute of Technology, 2007.

[110] Y. Gao, H. Shen, J. Cao, D. Li, and D. Yang, “Control of the formation and luminescent properties of polymorphic erbium silicates on silicon,” *Opt. Mater. Express*, 2019.